

Vol3 No2
July 2023
e-ISSN: 2682-9177

AJMed TECH ASIAN JOURNAL OF MEDICAL TECHNOLOGY

<https://doi.org/10.32896/ajmedtech.v3n2>



<https://ajmedtech.com>

eISSN 2682-9177



9 772682 917006

Editorial Team

Editor-in-Chief

Prof. Dr. Ahmad Sobri Muda (Malaysia); Medical
Assoc. Prof. Ir. Ts. Dr. Abdul Rahim Abdullah (Malaysia); Technology

Managing Editor

Ts. Dr. Norhashimah Mohd Saad (Malaysia)
Assoc. Prof. Dr. Noramaliza Mohd Noor (Malaysia)

Editorial Board

Ir. Dr. Anis Suhaila Shuib (Malaysia)
Dr. Norihan Abdul Hamid (Malaysia)
Assoc. Prof. Dr. Wira Hidayat Mohd Saad (Malaysia)
Dr. Norhidayah Mohamad Yatim (Malaysia)
Dr. Anas Tharek (Malaysia)
Mr. Adam Samsudin (Malaysia)
Mrs. Kamilah Jaffar (Malaysia)
Dr. Mohd Hatta Jopri (Malaysia)
Dr. Ezreen Farina Shair (Malaysia)

ASIAN JOURNAL OF MEDICAL TECHNOLOGY

Contents

Volume 3

Number 2

July 2023

No. Title Page

Original Article

- 1. HIGH PERFORMANCE THROUGH WALL HUMAN ACTIVITY RECOGNITION USING WIFI**
E. Abuhoureyah, Y.C Wong, M.I Ahmad Sadhiqin, J.H Chuah.....1
- 2. PRECISION AND RELIABILITY: CALIBRATION COEFFICIENTS AND LONG-TERM STABILITY ANALYSIS OF RADIOTHERAPY DOSIMETERS CALIBRATED BY SSDL, NUKLEAR MALAYSIA**
N. Abdullah, N. Mohd Noor, M. T. Dolah, J. K. Sangau.....15
- 3. DEVELOPMENT OF AN IoT-BASED KNEE EXOSKELETON DEVICE FOR REHABILITATION THERAPY MONITORING**
T.T.R. Thomas, M. R. Sapiee, M. H. Marhaban², A. J. Ishak², M. F. Miskon.....33
- 4. DOSE MAP BLOOD IRRADIATOR DOSIMETRY SYSTEM: CUSTOMIZED BLOOD EQUIVALENT PHANTOM AND GAFCHROMIC EBT-XD FILM**
A.S.Fazad, N.M.Noor, M.A.Nasir.....44

HIGH PERFORMANCE THROUGH WALL HUMAN ACTIVITY RECOGNITION USING WIFI

Fahd Abuhoureyah¹, Yan Chiew Wong^{1*}, Ahmad Sadhiqin bin Mohd
Isira¹, Joon Huang Chuah²

¹Centre for Telecommunication Research and Innovation (CETRI)
Fakulti Kejuruteraan Elektronik dan Kejuruteraan Komputer (FKEKK), Universiti
Teknikal Malaysia Melaka (UTeM), 76100 durian Tunggal, Melaka, Malaysia

²Department of Electrical Engineering, Faculty of Engineering, University of Malaya,
50603 Kuala Lumpur, Malaysia

*Corresponding Author's Email: ycwong@utem.edu.my

Article History: Received March 10, 2023; Revised May 12, 2023;
Accepted May 27, 2023

ABSTRACT: Passive human activity recognition without requiring a device is crucial in various fields, including smart homes, health care, and identification. However, current systems for human activity recognition require a dedicated device, or they need to be more suitable for scenarios where signals are transmitted through walls. To address this challenge, we propose a device-free, passive recognition system of human activity that utilizes CSI-based WiFi signals and does not require any dedicated devices. The proposed approach uses two techniques to distinguish different human activities. First, we introduce an opposite robust method to eliminate the influence of the background environment on correlation extraction and to obtain the correlation between human activity and its resulting changes in channel state information values. Second, we propose a normalized variance sliding windows algorithm to segment the time of human action from the waveforms, which can differentiate human actions' start and end times. We also implemented a CSI-based model using Nexmon with an LSTM algorithm with commodity WiFi devices and evaluated it in several environments. Our experimental results demonstrate that we achieve an average accuracy of 95% when signals pass through concrete walls.

KEYWORDS: *Through wall HAR, WiFi Sensing, Passive Device-Free HAR, CSI HAR.*

1.0 INTRODUCTION

Human activity recognition is a fundamental research topic in pervasive computing and human-computer interaction. It has the potential to support many emerging applications such as smart homes, augmented reality, identification, and health care. Different human activity recognition systems have been proposed with various techniques, including wearable sensor-based, computer vision-based, and ambient device-based approaches [1]. Wearable sensor-based methods utilize sensors, RFID [2], smartphones, and other devices to recognize human activities [3]. These systems use active detection techniques and require the device to be always on the body. On the other hand, computer vision-based approaches use cameras to capture image sequences and recognize human activities using activity classification algorithms [4]. However, the illumination of lights and shelters, such as walls, affects the camera, which limits its effectiveness.

Ambient device-based approaches attempt to recognize human activities using radar, infrared, audio, and other sensors. While these techniques do not require wearing or carrying anything on the body, some dedicated devices should be deployed. Recently, WiFi signals-based human activity recognition techniques have been widely studied. These techniques exploit Channel State Information (CSI) and multi-antennas techniques to distinguish different activities, such as E-eyes [5], CARM [6], WifiU, RT-Fall [7], and others. These systems have the advantages of passive detection and easy deployment, but they did not consider human activity recognition under scenarios where WiFi signals pass through walls [8].

HAR through walls using WiFi is a promising method because it provides a non-invasive and low-cost way to monitor human activities. WiFi signals penetrate walls and objects, allowing them to be used to sense the presence and movement of humans in indoor environments. The technique relies on analyzing the changes in the wireless signals as they interact with the human body and surrounding objects. Various signal processing and machine learning techniques are applied to extract features from the received signal, which classify human activities such as walking, running, sitting, or standing [4].

To realize the system, we face two main technical challenges. The

first challenge is to obtain beneficial human activity CSI correlation from the raw CSI measurements. It is a challenging problem to get this correlation because the WiFi signals are affected severely by the wall and the indoor physical environment (e.g., reflection, diffraction, and scattering). These aspects cause the received signal to become weak and mix a large amount of complicated background environmental information. The second technical challenge is to segment activity from CSI waveforms. Existing work shows that the activity can be segmented easily. However, the changes in CSI waveform caused by some human activities are not noticeable when the WiFi signals pass through the wall.

We propose a robust LSTM approach to overcome these challenges to obtain the correlation between human activity and its resulting changes in CSI values. This proposal includes the correlation of the indoor background environment and noise, and if weakly affected by the environment. The contributions of our work are summarized as follows:

- The present work introduces a novel approach for human activity recognition without using any dedicated device by leveraging WiFi signals that can penetrate through walls. We employ CSI amplitude to recognize human activities with commodity WiFi devices through walls.
- The proposed system has been implemented using commercial WiFi devices with a singular transmitter and receiver. The proposed model achieves an average classification accuracy of 95% for HAR based on CSI signals passing through the wall.

2.0 RELATED WORKS

In recent decades, wireless detection has gained popularity as a contactless sensing technique that appeals to simplicity and manageable availability [9]. Likewise, signals can spread through walls, furniture, and doors, and they don't need a line of sight (LoS), allowing for more significant detection regions [8]. Numerous CSI and machine learning-based algorithms have been presented to correctly identify and count individuals in each coverage area of a WiFi sense. Most of these studies use 1-3 transmitters (Tx) and three reception antennas (Rx) and utilize different wireless network cards.

However, the network interface card NIC frequently has various

constraints due to the natural physical effects of the transmission process. A quick review of the literature shows research that utilizes CSI data derived from standard WiFi equipment, such as NICs, that provide a restricted number of data subcarriers and severely influence classification performance [10]. Moreover, NICs are typically utilized for networking tasks; therefore, their dependability might be greatly harmed if they were also employed for sensing.

Several research studies have investigated the field of human activity recognition through walls using WiFi signals, commonly referred to as "through wall human activity recognition using WiFi," resulting in various proposed systems such as WiVi [11], WiSee [12], E-eyes [5], CARM [6], and RT-Fall [7]. However, most of these systems are limited in their ability to recognize human activity through walls, as they either require specialized equipment or need to consider the scenarios where signals pass through obstacles.

WiVi [11], for instance, uses WiFi signals through walls to detect objects and human actions. Still, it requires using PCs instead of commercial WiFi devices and performs poorly in activity classification. E-eyes [5] uses commercial WiFi devices to monitor human activity with one transmitter and three receivers, which achieve in-place and walking activity recognition. CARM [6] exploits CSI-speed and CSI-activity models to recognize different activities. In contrast, RT-Fall[7], on the other hand, exploits both the amplitude and phase of CSI measurements to detect falls.

Despite the advantages of these systems, including passive detection and easy deployment, they do not consider the scenarios where signals pass through walls. In indoor environments, where multiple rooms may access one wireless signals AP, walls may block all the direct and reflected propagation paths between the receiver and the transmitter. The system exploits the differences in the CSI values measured to classify the activities of interest. This approach has the potential to significantly improve the accuracy and reliability of HAR systems in scenarios where signals pass through walls, making it suitable for a wide range of applications, including home automation, security, and healthcare.

3.0 METHODOLOGY

3.1 Primarily and problem analysis

CSI is widely used to capture activity data as it provides high

sensitivity to channel link variations and has a fine-grained nature and small size, as shown in equation (3.1) and a schematic network diagram.

$$y = Hx + n \tag{3.1}$$

In the equation, H is a complex matrix of CSI values, and n is the channel noise [13]. The MIMO system utilizes multiple channels to increase transmission rates by constructing a matrix of connection links represented as: -

$$H_i = \begin{bmatrix} h_i^{11} & h_i^{12} & \dots & h_i^{1N_T} \\ h_i^{21} & h_i^{22} & \dots & h_i^{2N_T} \\ \vdots & \vdots & \vdots & \vdots \\ h_i^{N_R1} & h_i^{N_R2} & \dots & h_i^{N_RN_T} \end{bmatrix} \tag{3.2}$$

The CSI measures the amplitudes and phases influenced by the paths and the number of amplitudes and phase shifts. Therefore, each CSI entry corresponds to the channel frequency response, as shown in equation (3.3).

$$h(f) = \sum_{l=1}^N \alpha_l \exp^{-j2\pi f \tau_l} \tag{3.3}$$

The CSI ratio of WIFI indicates the impact of objects in the environment on the transmission of OFDM signals, causing signal weakening and scattering [14], [15]. This rapidly amplifies human motion's effect on the phase variation, as expressed mathematically in equation (3.4) as:

$$H(f, t) = \delta(t) e^{-j\phi(t)} \sum_{l=1}^L A_l(t) e^{-j2\pi \frac{d_l(t)}{\lambda}} \tag{3.4}$$

Whereby $\delta(t)$ represents the intensity of impulsive noise, and $\phi(t)$ represents the time-varying phase offset. L represents the total number of propagating routes, λ represents the wavelengths, and $A_l(t)$ and $d_l(t)$ represent the signal's attenuation and the L pathway's length, respectively.

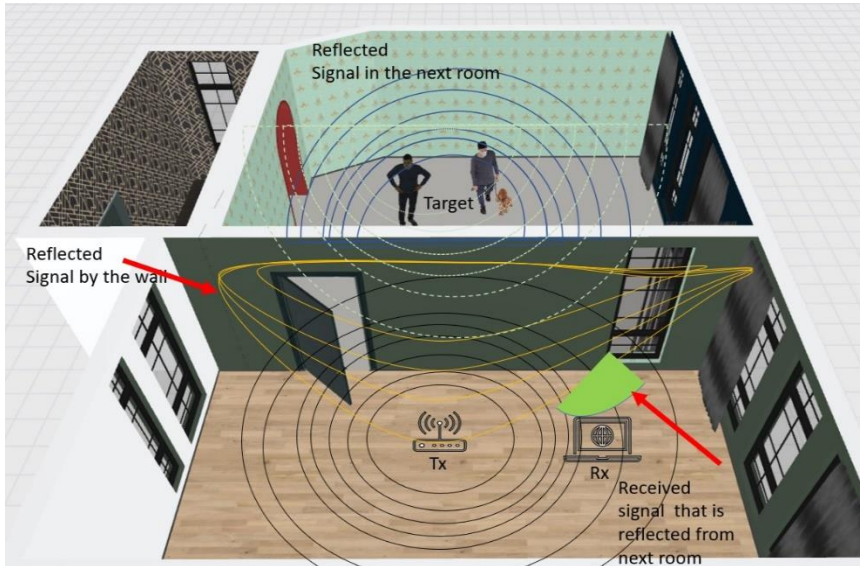


Figure 1: The utilization of WiFi for human activity recognition through walls demonstrates the presence of weak reflected signals

The analysis of activities, as depicted in Figure 1, confirms exceptional diversity in packet transmission through the wall. One of the main challenges is the complex and unpredictable propagation of wireless signals through the wall, which can cause severe signal attenuation, reflection, and multipath effects. Another challenge is collecting and processing high-quality CSI data due to commercial WiFi devices' limited bandwidth and sensitivity. Additionally, there is a need to develop robust and accurate algorithms to extract meaningful features from the CSI data and classify different human activities under various scenarios and environments.

$$P_R = \frac{G_T G_R P_T \lambda^2 \sigma F}{(4\pi)^3 R} \quad (3.5)$$

The provided equation considers the received power (P_R), transmitted power (P_T), the gain of transmission (G_T), and receiving (G_R), as well as the distance (R) that signals need to travel across the wall and the amount of power that is reflected into the adjacent room, where only a small fraction of power is reflected to the receiver with a cross-sectional area of σ . Moreover, environmental factors, represented by F , significantly affect the equation. In the proposed model, the reflected power within the same room is removed, and attention is given to the body effects in the adjacent room.

3.2 System Overview

The proposed system has two WiFi devices serving as a transmitter and receiver. A commercially available WiFi access point with one antenna is the transmitter, while a common wireless NIC is the receiver. The experiments used a TP-Link EC230-g1 as the transmitter and a Raspberry Pi 4b as the receiver. The AP and receiver are placed in different adjacent rooms, and the wall obstructs all direct and reflected propagation paths between them. If human activity occurs in either the transmitter or receiver room, the system can automatically detect it. Figure 2 illustrates the system's principle of operation.

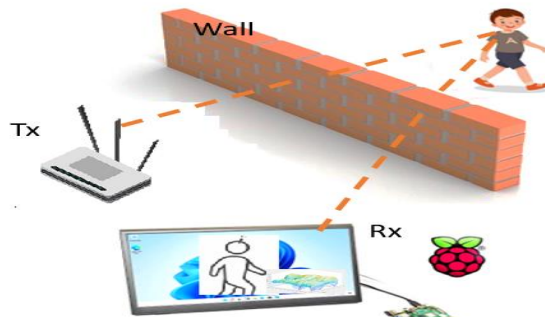


Figure 2: System illustration of human activity recognition when the signals pass through the wall

The methodology of the system is described in this work through a flow chart consisting of four main stages: data collection, pre-processing, feature extraction, and classification. The data collection process involves using a Raspberry Pi device connected to Nexmon firmware to capture raw data of activities in the adjacent room. The proposed approach is focused on predicting activities through walls using wide-angle views. The captured data is subjected to various techniques for extraction and filtering, such as FFT, Hampel, and median, to eliminate noise for visualization and training purposes. The feature extraction stage involves extracting meaningful features from the pre-processed data to represent the activities accurately. Finally, a three-layer LSTM network with sequential connections and SoftMax function is employed for activity recognition and classification.

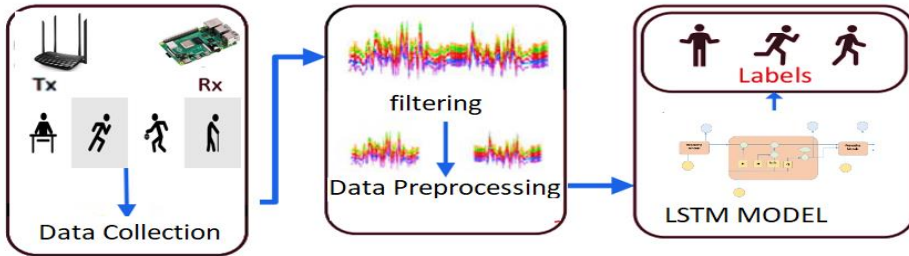


Figure 3: System Architecture

3.3 Location Correlation with Extraction

We employed the median of Hampel filter processes to denoise matrix signals. The median filter is a nonlinear digital filtering technique that replaces each pixel value in a signal with the median value of its neighboring values. This filter effectively removes salt-and-pepper noise, a common type of noise in the signal. On the other hand, the Hampel filter process is a robust method for outlier detection that uses a sliding window to detect outliers in a movement. It replaces the outlier value with the median value of the window. Combining these two filters effectively reduces noise in matrix signals while preserving the integrity of the underlying data. By applying these denoising techniques, we improved the accuracy of signal analysis and interpretation shown in Figure 4.

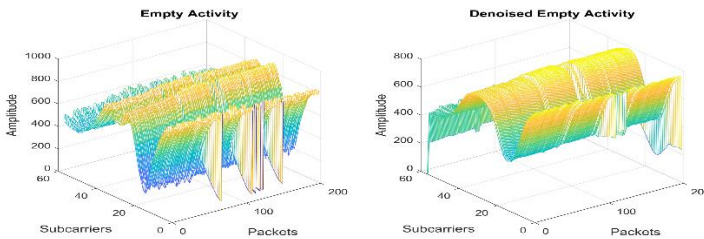


Figure 4: Denoising signal

As a person moves, their body reflects and scatters the wireless signals, causing variations in the CSI values. By analyzing these variations, it is possible to identify specific human activities such as walking, sitting, or standing shown in Figure 5. One advantage of using CSI signals for activity recognition is that they are non-intrusive and do not require wearable sensors. Additionally, they can be collected using commodity WiFi devices, making the approach cost-effective and widely accessible. By leveraging the amplitude changes in CSI signals caused by body movement

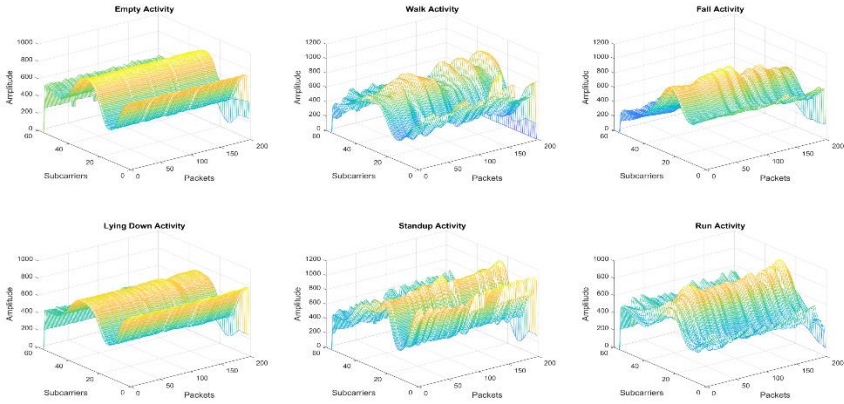


Figure 5: Human activity recognition when the signals pass through the wall

It was observed that the activity recognition system proposed in the research could not capture reflected signals from the next room, as evidenced by equation 5. As a result, it was necessary to separate the activity from the initial room signal reflections to achieve accurate activity recognition. This separation was achieved using a signal processing technique that effectively filters unwanted reflections and isolates the relevant activity signal shown in Figure 6.

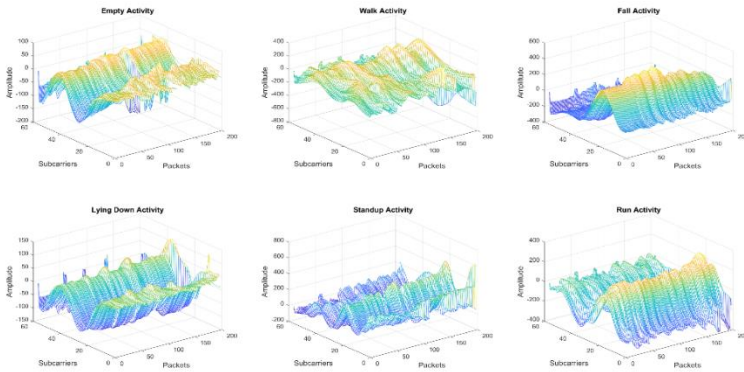


Figure 6: Raw CSI amplitude environmental separation results

4.0 IMPLEMENTATION AND EVALUATION

4.1 Implementation

In this work, the Raspberry Pi 4B was employed to capture data and to evaluate the performance of the activity recognition model for through-wall sensing of six different activities (empty, lying, walking, running, standup, and falling). The Raspberry Pi was set to

monitoring mode at 20 MHz and 80 MHz at 2.4 GHz/5 GHz, respectively, using a transmitter (Tx) (TP-LINK router) and a receiver (Rx) Raspberry Pi 4b, both of which utilized omnidirectional antennas. Furthermore, data injection was necessary, for which the Lenovo G580 laptop was used to inject the router in these experiments to achieve flow data in monitoring mode. The data is collected in the first stage using Wireshark/TCPDUMP in the monitoring mode of Nexmon installed on the Raspberry Pi.

4.2 Experimental Setup

The evaluation was implemented in the lab environment shown in Figure 7 to investigate the wider-angle model in different aspects, such as frequency, distance, and angle. The figure is divided into five positions, each subject to six regular activities. The study is conducted using both 2.4 GHz frequencies. The distance between the transmitter and the router is 2 meters, and the spaces between the receiver and the different positions are labeled in Figure 7.



Figure 7: Layout of evaluation location

4.3 Human Activity Recognition

The experimental results demonstrate that the proposed system can recognize human activities through a wall, as illustrated in Figure 8. The model achieved this by classifying the separated signal using

machine learning techniques, including low-rank matrix decomposition, feature extraction, and an LSTM neural network. These techniques enabled the model to extract relevant features from the raw signal and learn the temporal dependencies in the signal, resulting in accurate recognition of the target activities.

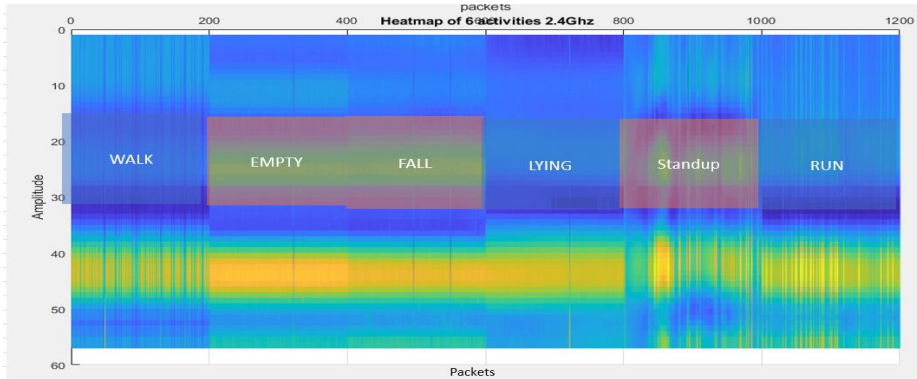


Figure 8: Activity classification

With high accuracy, the system could classify six activities, including empty, lying, walking, running, standing up, and falling, with a few samples shown in the confusion matrix in Figure 9.

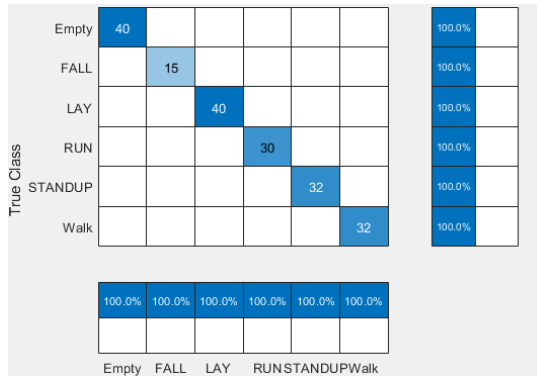


Figure 9: Confusion matrix of through wall HAR using 2.4GHz WiFi

The models exhibited remarkable proficiency in identifying human activities through walls via WiFi signals in five distinct locations, as presented in Table 1. The implications of these findings are substantial, particularly for fields such as security and surveillance, healthcare, and home automation.

Table 1: The efficacy of activity detection through a wall in five positions is shown in Figure 7.

Freq	2.4Ghz				
	Position 1	Position 2	Position 3	Position 4	Position 5
Empty	100	100	100	100	100
Fall	100	40	100	100	100
Lie Down	77.5	92.5	80	100	85
Run	100	96.7	96.7	96.7	96.7
Sit-down	96.7	96.7	96.7	80	96.7
Walk	100	100	96.7	96	100
Acc.%	94 %	92.4%	85%	95%	95.6%

5.0 CONCLUSION

The proposed model provides a narrative approach to improve the forecasting of through-wall human activities through signal processing in human activity recognition systems. Using the CSI signals captured through the wall, we showed that the proposed system accurately classified six activities (empty, lying, walking, running, sitting down, and falling). We also demonstrated the effectiveness of the system in different positions and angles, which can provide valuable insights for real-world deployment. The proposed approach is low-cost and easy to implement, making it suitable for various applications. The results of this study suggest that CSI-based HAR using WiFi and LSTM can be a viable solution for activity recognition through walls, with potential applications in healthcare, security, and intelligent home systems. Further research can explore the feasibility of using this system in larger spaces with more complex activities. Future research will focus on refining the localization and data extraction algorithm with enhanced technologies such as beamforming and array antennas.

6.0 ACKNOWLEDGMENTS

This work was initially accepted for and presented at ICTEC2022. The authors acknowledge the technical and financial support by Universiti Teknikal Malaysia Melaka (UTeM), Malaysia, and the Ministry of Higher Education, Malaysia, under the research grant no FRGS/1/2020/ICT02/UTEM/02/1

7.0 REFERENCES

- [1] C. Shi *et al.*, "Demo: Device-free Activity Monitoring Through Real-

- time Analysis on Prevalent WiFi Signals," *2019 IEEE Int. Symp. Dyn. Spectr. Access Networks, DySPAN 2019*, pp. 1–2, 2019.
- [2] H. Obeidat, W. Shuaieb, O. Obeidat, and R. Abd-Alhameed, *A Review of Indoor Localization Techniques and Wireless Technologies*, vol. 119, no. 1. Springer US, 2021.
- [3] Y. Zhang, Y. Yin, Y. Wang, J. Ai, and D. Wu, "CSI-based location-independent Human Activity Recognition with parallel convolutional networks," *Comput. Commun.*, vol. 197, no. November 2022, pp. 87–95, 2023.
- [4] X. Wu, Z. Chu, P. Yang, C. Xiang, X. Zheng, and W. Huang, "TW-See: Human activity recognition through the wall with commodity WiFi Devices," *IEEE Trans. Veh. Technol.*, vol. 68, no. 1, pp. 306–319, 2019.
- [5] Y. Wang, J. Liu, Y. Chen, M. Gruteser, J. Yang, and H. Liu, "E-eyes: Device-free location-oriented activity identification using fine-grained WiFi signatures," *Proc. Annu. Int. Conf. Mob. Comput. Networking, MOBICOM*, no. October 2015, pp. 617–628, 2014.
- [6] W. Wang, A. X. Liu, M. Shahzad, K. Ling, and S. Lu, "Device-Free Human Activity Recognition Using Commercial WiFi Devices," *IEEE J. Sel. Areas Commun.*, vol. 35, no. 5, pp. 1118–1131, 2017.
- [7] T. Z. Chowdhury, "Using WiFi channel state information (CSI) for human activity recognition and fall detection," no. April, pp. 24–50, 2018.
- [8] S. Di Domenico, M. De Sanctis, E. Cianca, and M. Ruggieri, "WiFi-based through-the-wall presence detection of stationary and moving humans analyzing the doppler spectrum," *IEEE Aerosp. Electron. Syst. Mag.*, vol. 33, no. 5–6, pp. 14–19, 2018.
- [9] J. Li, K. Yin, and C. Tang, "Slideaugment: A simple data processing method to enhance human activity recognition accuracy based on WiFi," *Sensors*, vol. 21, no. 6, pp. 1–13, 2021.
- [10] Q. Li, R. Gravina, Y. Li, S. H. Alsamhi, F. Sun, and G. Fortino, "Multi-user activity recognition: Challenges and opportunities," *Inf. Fusion*, vol. 63, no. March, pp. 121–135, 2020.
- [11] L. Zhang, X. Ruan, and J. Wang, "WiVi: A Ubiquitous Violence Detection System with Commercial WiFi Devices," *IEEE Access*, vol. 8, pp. 6662–6672, 2020.
- [12] S. Ajmera, N. Chouhan, and N. Audeechya, "Wisee Technology," pp. 264–267, [Online]. Available: www.ijert.org
- [13] M. Liyanage, C. Chang, S. Srirama, and S. Loke, "Indoor people density sensing using WiFi and channel state information," *Adv. Model. Anal.*

- A, vol. 61, no. 1, pp. 37–47, 2018.
- [14] Y. Zeng, D. Wu, J. Xiong, and D. Zhang, "Boosting WiFi Sensing Performance via CSI Ratio," *IEEE Pervasive Comput.*, vol. 20, no. 1, pp. 62–70, 2021.
- [15] Y. He, Y. Chen, Y. Hu, and B. Zeng, "WiFi Vision: Sensing, Recognition, and Detection with Commodity MIMO-OFDM WiFi," *IEEE Internet Things J.*, vol. 7, no. 9, pp. 8296–8317. 2020.

PRECISION AND RELIABILITY: CALIBRATION COEFFICIENTS AND LONG-TERM STABILITY ANALYSIS OF RADIOTHERAPY DOSIMETERS CALIBRATED BY SSDL, NUKLEAR MALAYSIA

N. Abdullah^{1,2*}, N. Mohd Noor^{1,3}, M. T. Dolah⁴ and J. K. Sangau⁴

¹Medical Physics Laboratory, Department of Radiology, Faculty of Medicine and Health Sciences, Universiti Putra Malaysia, 43400 Serdang, Selangor, Malaysia.

²Medical Physics Laboratory, Radiation Metrology Group, Radiation Safety and Health Division, Malaysian Nuclear Agency, 43000 Kajang, Selangor, Malaysia.

³Medical Physics Unit, Hospital Sultan Abdul Aziz Shah, Universiti Putra Malaysia, 43400 Serdang, Selangor, Malaysia.

⁴Secondary Standard Dosimetry Laboratory, Radiation Metrology Group, Radiation Safety and Health Division, Malaysian Nuclear Agency, 43000 Kajang, Selangor, Malaysia.

*Corresponding Author's Email: noramaliza@upm.edu.my

Article History: Received Jun 22, 2023; Revised July 19, 2023;
Accepted July 20, 2023

ABSTRACT: One of the main objectives of the Secondary Standard Dosimetry Laboratory (SSDL) in radiotherapy dosimetry is verifying the radiation dose provided to patients is accurate and meets globally recognised standards. Properly calibrating the therapy dosimeters used in the radiotherapy centres is the first step the SSDL must take to ensure this goal is attained. This study analyses the calibration coefficients and long-term stability of therapy dosimeters calibrated by Nuklear Malaysia's SSDL. The dosimeters were calibrated in the absorbed dose to water using ⁶⁰Co gamma rays, following the procedure described in IAEA TRS No. 398 and IAEA TRS No. 469. Two hundred therapy dosimeters from 33 radiotherapy centres were evaluated for the percentage deviation of the calibration coefficients provided by the SSDL and the manufacturer. Furthermore, the variation in calibration coefficient and the long-term stability of therapy dosimeters from 2011 to 2021 were examined. The percentage deviation of calibration coefficients between the SSDL and manufacturers found that most (82%) user dosimeters were

within the IAEA's acceptance limit of $\pm 1.5\%$. Overall, the stability of calibration coefficient values ranged between 33.25% and -27.24%, with an average of 0.03%. As predicted, only 15% of the therapy dosimeters fulfill the criteria for long-term stability of 0.5%. In conclusion, proper maintenance and annual calibration of therapy dosimeters are very important to improve accuracy, minimise measurement uncertainty, and thus reduce the likelihood of errors in radiotherapy dosimetry.

KEYWORDS: *Absorbed dose to water; calibration coefficient; long-term stability; radiotherapy dosimeter; SSDL.*

1.0 INTRODUCTION

According to the Malaysia National Cancer Registry Report, the number of newly diagnosed cancer cases in the nation has significantly increased over the previous five years [1]. Between 2012 and 2016, breast, colorectal, and lung cancers have been the most frequently reported cancers, with males having a lifetime risk of 1 in 10 and females of 1 in 9. Overall, there were 48,639 new cancer cases recorded in Malaysia in 2020, according to the World Health Organization, and the cancer incidence in Malaysia is expected to double by 2040 [2]. With the rising prevalence of cancer, the demands for radiotherapy will be rising and thus require the establishment of high-quality and safe radiotherapy [3]. There are currently 35 radiotherapy centres in the country, of which 7 are government hospitals, and 28 are private facilities [4]. One government-funded radiotherapy service is delivered through a contract with a private institution. In total, there are 92 radiation therapy modalities, including 58 medical linear accelerators, 19 brachytherapy, 7 intra-operative radiotherapy (IORT), 5 tomotherapy and 1 cyberknife [5]. One of the fundamental objectives of the Secondary Standards Dosimetry Laboratory (SSDL) in radiotherapy dosimetry is to confirm that the dose given to patients undergoing radiation treatment is accurate and consistent with the acceptance level of $\pm 5\%$, as stipulated in the International Commission on Radiation Units and Measurements (ICRU) Report 24 [6]. Subsequently, the first step to achieving this goal is to deliver traceable calibrations of radiation-measuring instruments used in radiotherapy centres.

The SSDL of the Malaysian Nuclear Agency (Nuklear Malaysia) plays its prime function as the National Centre for Radiation

Metrology. Regarding this, the SSDL provides calibration services for calibrating radiation-measuring instruments used in various fields, including diagnostic radiology, radiation therapy, and radiation protection. These services have been accredited with the Malaysian Standard (MS) ISO/IEC 17025 [7] under the Laboratory Accreditation Scheme of Malaysia (SAMM No.: 275) since 2004 [8]. In Malaysia, the calibration of radiation-measuring instruments is required in compliance with the regulations under the Laws of Malaysia, including the Atomic Energy Licensing Act 1984 (Act 304), Occupational Safety and Health Act 1994 (Act 514) and the National Measurement System Act 2007 (Act 675). Generally, the regulations specified under these laws seek to ensure the accuracy of measurement and thereby contribute to the goal of radiation safety and protection for workers, patients, and members of the public. Apart from domestic services, SSDL also has the trust of private companies abroad to serve calibration services. By 2023, various companies from Brunei Darussalam, Indonesia, India, Philippines, Singapore, Thailand, and the United Arab Emirates have received calibration services from the SSDL.

Two publications have reported on the accuracy and stability of the therapy dosimeters used in Malaysian radiotherapy centres. The first study by [9] evaluated the calibration coefficients for 29 therapy dosimeters belonging to 16 radiotherapy centres calibrated using a ^{60}Co beam in the SSDL for seven years (2004 to 2010). The findings of the study showed that the calibration coefficients for the dosimeters are reliable for measuring patient dose and do not vary over time. These results were in agreement with the study of 38 therapy dosimeters used in 14 Polish radiotherapy centres [10]. The second study presented the analysis of calibration coefficients for 33 therapy dosimeters from 24 Malaysian radiotherapy centres calibrated from 2004 to 2012 [11]. The results are contrary to the previous research, as the study indicates that there were systematic errors in the calibration coefficients over these periods of observations for various models of therapy dosimeters. The relatively large sample size of calibration coefficients (6474 dosimeters) obtained from the three accredited dosimetry calibration laboratories (ADCLs) operating in the United States, [12] revealed that the calibration coefficients for older dosimeters are more variable than those manufactured more recently. There are consistent findings for these studies, which found a significant dispersion of calibration coefficients of particular therapy dosimeters due to manufacturing

differences [10]–[12].

This present work highlights the latest data on therapy dosimeters from Malaysian radiotherapy centres calibrated at the SSDL from 2011 to 2021. The purposes of this work are: (i) to observe the availability of calibrated therapy dosimeter in the SSDL; (ii) to compare the deviation of the calibration coefficient in terms of absorbed dose to water provided by the SSDL and manufacturer; (iii) to investigate the variation of the calibration coefficients of therapy dosimeters over a certain period concerning different manufacturers; and (iv) to examine the long-term stability of these therapy dosimeters after being calibrated several times from 2011 to 2021.

2.0 METHODOLOGY

2.1 Calibration of Radiation Therapy Dosimeters

Therapy dosimeters from various radiotherapy centres (user dosimeters) were calibrated in the SSDL in terms of the absorbed dose to water in ^{60}Co gamma rays, type Eldorado 8 (Nordion, Ottawa, Canada). The determination of the absorbed dose to water was performed according to the Technical Report Series (TRS) No. 398 provided by the International Atomic Energy Agency (IAEA) [13]. The user dosimeters were calibrated against the SSDL working standard dosimeter (SSDL dosimeter) in accordance with the calibration procedure of the IAEA TRS No. 469 [14]. In all measurements, both dosimeters were positioned accurately at 5 g/cm² depth in water phantom with a 10 cm × 10 cm field size at the water phantom surface, and a source-surface distance (SSD) of 80 cm (Figure 1). The dosimeter reference point was ensured to be placed accurately at the central axis of the radiation beam. Laser lights were utilised as a guide to ease the dosimeter alignment. The water tank, with a dimension of 300 mm × 300 mm × 300 mm, was used to provide a full scatter radiation condition. To meet the IAEA Code of Practice for ^{60}Co irradiation, the water tank with a window dimension of 100 mm × 100 mm × 2 mm for the horizontal beam was used [13]. A protective sleeve was utilised for the non-waterproof dosimeters. This sleeve was designed with a 2 mm thickness to allow the dosimeter to reach thermal equilibrium with the water in less than 10 minutes and a 2 mm air gap to allow the chamber air pressure to quickly reach the ambient air pressure. The water tank and waterproof sleeve were made of polymethylmethacrylate (PMMA) with a density of 1.19 g/cm³.

The SSDL dosimeter used in the calibration has traceability to the SSDL reference standard dosimeter, which was sent for recalibration at the IAEA Dosimetry Laboratory every three years. The periodic stability checks of the SSDL reference and working standard dosimeters were performed every four months using the ^{90}Sr source. These checks are necessary to maintain confidence in the performance of the SSDL dosimeters between calibration intervals.



Figure 1: Set-up for therapy dosimeter calibrations in terms of absorbed dose to water

Before irradiating the user dosimeter, the current absorbed dose to water rate of SSDL standard dosimeter was calculated from the value established at a reference date, taking into account the radioactivity decay of the ^{60}Co source using Equation (1).

$$\dot{D}_c = \dot{D}_r e^{\frac{-0.693t}{T_{1/2}}} \quad (1)$$

Where \dot{D}_c and \dot{D}_r indicate the current and reference absorbed dose to water rate from the ^{60}Co source, t is a time difference (in days) between two dose rate measurements and $T_{1/2}$ is a half-life of the ^{60}Co source with 1925.20 ± 0.25 d [15].

The calibration was carried out in a controlled environment with a room temperature between $23^\circ\text{C} \pm 5^\circ\text{C}$, relative humidity between 20%

and 70%, and normal atmospheric pressure to ensure reproducible results. These parameters were measured prior to and post irradiations using a traceably calibrated thermometer, hygrometer, and barometer. The thermometer was inserted well into the water phantom and hygrometer, while the barometer was placed at the control panel. The dosimeters were allowed to warm up for at least 30 minutes to ensure stability and acclimatise the dosimeter to the ambient conditions. In addition, the dosimeter's polarising potential, leakage, and radiation-induced leakage currents were verified. The leakage should be less than 0.1% of the current (nC) during measurements [14]. At least five readings were taken for each dosimeter, and the calculated standard deviation of the reading was ensured to be less than 0.1% for the SSDL dosimeter and less than 0.2% for the user dosimeter. Using the reference of temperature, $T = 20\text{ }^{\circ}\text{C}$, and atmospheric pressure, $P = 101.325\text{ kPa}$, the correction for temperature and pressure was calculated. The result of calibration in terms of the absorbed dose to water calibration coefficient, $N_{D,w}$ in mGy/nC was determined as the ratio of the absorbed dose to water rate in mGy/s obtained from the SSDL working standard dosimeter, and the reading of the user dosimeter in nC/s. The calibration results are valid for 12 months [16].

2.2 Analysis of calibration coefficient provided by the SSDL and manufacturer

Typically, the client sends the new therapy dosimeter to the SSDL for calibration along with the calibration certificate provided by the manufacturer. Using this information, the percentage deviation of the calibration coefficient between SSDL and the manufacturer was calculated using Equation 2. The IAEA has set an acceptance limit of 1.5% for the results of these comparisons [14]. Considering the measurement uncertainty in the SSDL, users with results outside the limit of 2% will be not issued the calibration certificate. They were also advised to take further action to resolve the discrepancy.

$$\text{Deviation (\%)} = \frac{N_{D,w}(\text{SSDL}) - N_{D,w}(\text{manufacturer})}{N_{D,w}(\text{manufacturer})} \times 100 \quad (2)$$

2.3 Analysis of calibration coefficients of therapy dosimeters over years

The variation of the calibration coefficients of therapy dosimeters over a particular time for different manufacturers was investigated. The stability of a therapy dosimeter was determined by comparing the

calibration coefficient from the subsequent calibration, $N_{(D,w)i}$ to the calibration coefficient from the previous calibration, $N_{(D,w)i-1}$. The equation used to calculate the stability of the calibration coefficient is shown in Equation 3. The dosimeters that were first-time calibrated in the SSDL will be not included in the calculation. According to IAEA Report 469 [14], the stability check of the calibration coefficient should not be changed more than around 0.3% from the value assigned at the most recent calibration. If not, the dosimeter should be sent for repair and/or recalibration as soon as possible.

$$\text{Stability check (\%)} = \frac{N_{(D,w)i} - N_{(D,w)i-1}}{N_{(D,w)i-1}} \times 100 \quad (3)$$

Where i denotes a subsequent calibration of the total number of calibrations.

2.4 Analysis of long-term stability of user dosimeter

The long-term stability of user dosimeters was examined based on their calibration coefficients for the absorbed dose of water, $N_{D,w}$ in ^{60}Co gamma radiation. In this work, the long-term stability was estimated for each dosimeter as a mean calibration coefficient over the total period of the calibration service in SSDL. The long-term stability, $\bar{\delta}_{N(D,w)}$ was determined using the following Equations 4 and 5 [10].

$$\bar{\delta}_{N(D,w)} = \frac{1}{\tau} \sum_{i=1}^{n-1} \left(\frac{|N_{(D,w)i+1} - N_{(D,w)i}|}{N_{(D,w)1}} \right) \quad (4)$$

Where

$$\tau = \sum_{i=1}^{n-1} (t_{i+1} - t_i) \quad (5)$$

The i -th index represents subsequent calibrations out of a total of n calibrations. In equation 4, the modulus of changes of $N_{(D,w)}$ between subsequent calibrations, relative to the first $N_{(D,w)1}$ value, is summed and divided by a period, τ which is the sum of time intervals between the subsequent calibrations. The calibration coefficient should be stable within 0.5% over many years [14]. The correlation between long-term

stability with the: (i) year of calibration; and (ii) manufacturer of the dosimeter was further assessed using the IBM SPSS Statistics Version 27.

3.0 RESULTS AND DISCUSSION

3.1 Distribution of calibrated therapy dosimeter

From 2011 to 2021, the SSDL received approximately 90 therapy dosimeters per year from 33 radiotherapy centres, including 23 private, 6 government, and 4 university hospitals. As seen in Figure 2, there was a significant increment in the number of dosimeters calibrated in the SSDL from 2011 to 2020. It is most likely due to the increased number of radiation centres in Malaysia throughout these times. The highest number of 133 dosimeters calibrated was recorded in 2020, with 122 (92%) dosimeters sent for recalibration and 11 (8%) dosimeters calibrated for the first-time. Even during the period of the COVID-19 pandemic from 2019 to 2021, we found that the return rate of dosimeters for recalibration was considered high within these periods. This situation described the medical physicist's awareness of the need to provide accurate radiotherapy to treat patients in a high-quality and safe manner. However, in 2021, as predicted, the number of dosimeters calibrated declined as a result of the Ministry of Health Malaysia's decision to extend the validity of calibration certificates to 60 days after the expiry date during the COVID-19 pandemic's Movement Control Order.

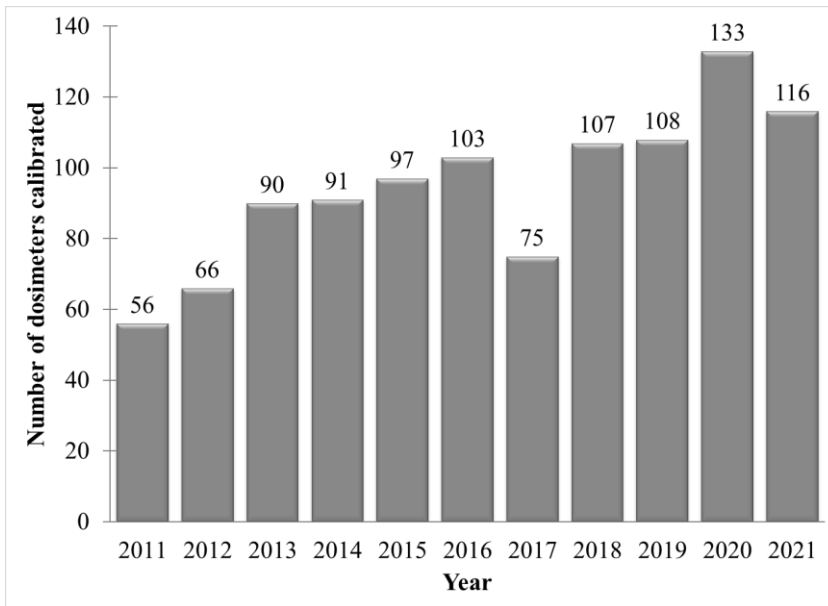


Figure 2: The number of therapy dosimeters calibrated from 2011 to 2021

Each radiotherapy centre generally has at least one therapy dosimeter to be used in routine linac quality assurance. From Figure 3, 21 radiotherapy centres have less than 6 therapy dosimeters, 9 have between 6 to 10 therapy dosimeters, and 4 have more than ten therapy dosimeters. The latter were government hospitals (3) and hospital universities (1) that we understand have many linacs installed and also a high workload for treatment and research activities. Therefore, they require several types of therapy dosimeters to support their work.

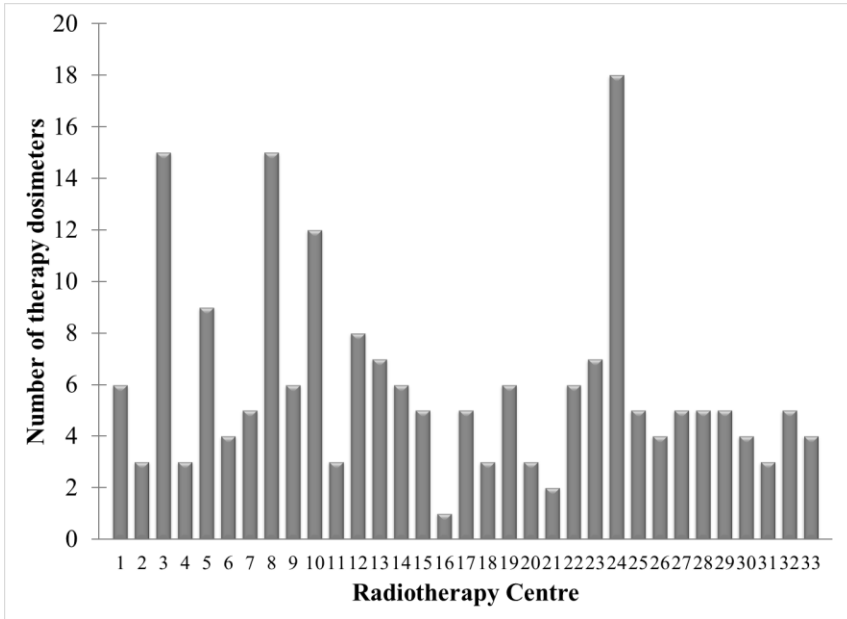


Figure 3: Number of therapy dosimeters belonging to Malaysian radiotherapy centres

3.2 Percentage deviation of SSDL and manufacturer calibration coefficients

Table 1 presents the results of the percentage deviation of calibration coefficients between the SSDL and manufacturer for user dosimeters that were first-time calibrated in the SSDL from 2010 to 2021. Most of the user dosimeters (82%) were within the IAEA's acceptance limit of $\pm 1.5\%$, while the Exradin dosimeters showed excellent results with all the dosimeters being within the acceptance limit. The user dosimeters manufactured by the PTW demonstrated that 88% of the dosimeters were within the acceptance limit, followed by NE and IBA manufactured dosimeters with 82% and 70%, respectively. These results revealed the crucial importance of calibration at local SSDL for the newly purchased therapy dosimeters before they were used in the radiotherapy centres [16]. Furthermore, Malaysia's high seasonal humidity compared to manufacturer countries may cause a significant relative response, particularly in an ionisation chamber with a hygroscopic wall [17]. A total of 170 calibration certificates (85%) were issued for the first-time calibration, and the remaining 30 dosimeters failed to get the certificate because they exceeded the SSDL's acceptance limit of $\pm 2\%$.

Table 1: The percentage deviation of calibration coefficients between the SSDL and manufacturer for user dosimeters that were first-time calibrated in the SSDL from 2010 to 2021

Manufacturer	Number of therapy dosimeters that were first-time calibrated in the SSDL from 2010 to 2021	Number of therapy dosimeters within the percentage deviation of SSDL and manufacturer calibration coefficients		
		$\pm 1.5\%$ ¹	$\pm 2.0\%$ ²	$> \pm 2.0\%$
Exradin	19	19	19	-
IBA	83	58	62	21
NE	6	5	5	1
PTW	92	81	84	8
Total	200	163	170	30

¹ IAEA's acceptance limit of $\pm 1.5\%$

² SSDL's acceptance limit of $\pm 2\%$

The study discovered the highest deviation between the SSDL and manufacturer calibration coefficients was given by the IBA dosimeter, at 130%. However, the result for this dosimeter was improved to 1.89% in the following year after corrective action was taken by the user. Overall, 10 dosimeters were observed to have better results within $\pm 2\%$ deviation in the second-year calibration. In contrast, the remaining dosimeters pushed the results outside the limit. The low radioactivity (3.2 TBq on 14 December 2022) of the ⁶⁰Co source used in the calibration was identified as one of the causes of this discrepancy. For convenience, the activity of the source should be sufficient to produce an air kerma rate of not less than 0.1 Gy/min at a distance of 1 m [14]. In addition, a few user dosimeters with technical specifications were not sensitive enough to detect the low radiation dose produced by the ⁶⁰Co source. To address this issue, the SSDL received a new ⁶⁰Co source with sufficient radioactivity this year (80.97 TBq on 18 August 2022).

3.3 Variation of calibration coefficient over years

The ratios of the calibration coefficient from the subsequent calibration, $N_{(D,w)j}$ to the calibration coefficient from the previous calibration, $N_{(D,w)j-1}$ for the therapy dosimeter calibrated in the SSDL from 2012 to 2021 is presented in Figure 4. The PTW manufactured dosimeters appeared to be the highest number of dosimeters within the IAEA's acceptance limit of $\pm 0.3\%$ with 33 dosimeters (42%), followed by IBA and Exradin dosimeters with 24 (33%) and 2 (17%). However, all NE dosimeters were observed to be outside the acceptable limit. Overall, the stability of calibration coefficient values ranged between 33.25% and -27.24%,

with an average of 0.03% (Table 2). These findings support the significant dispersion of calibration coefficients of particular therapy dosimeters due to manufacturing differences i.e. different types of dosimeters were constructed with different chamber dimensions. [12] and [10] reported a similar trend in their studies. The calibration coefficients of PTW 30013 and NE 2571 dosimeters exhibit the least variable, followed by the Exradin A12 calibration coefficients, while the Exradin A1SL revealed the most variation among calibration coefficients [12]. Significant dispersion of calibration coefficients of particular plane-parallel chambers was observed due to more complex chamber construction than cylindrical chambers [10].

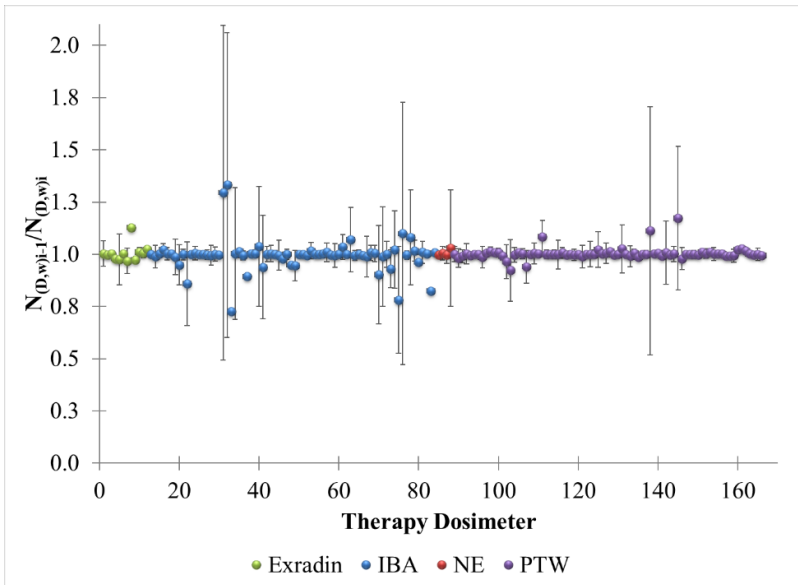


Figure 1: Ratio of the calibration coefficient from the subsequent calibration, $N_{(D,w)i}$ to the calibration coefficient from the previous calibration $N_{(D,w)i-1}$ for therapy dosimeter calibrated in the SSDL from 2012 to 2021. Error bars represent the standard deviation of the ratio

Table 2: The stability of calibration coefficients of therapy dosimeters for different manufacturers calibrated in the SSDL from 2012 to 2021

Manufacturer	Number of therapy dosimeters	Stability of calibration coefficients (%)			
		Mean	Std. Dev.	Min.	Max.
Exradin	12	0.57	4.20	-3.14	12.84
IBA	72	-0.47	7.82	-27.24	33.25
NE	4	0.71	1.61	-0.41	3.05
PTW	78	0.37	2.91	-7.69	17.31
Total	166	0.03	5.63	-27.24	33.25

It has appeared that some dosimeters have outlying calibration coefficients for a certain year of calibration, as depicted by the large error bars (Figure 5).

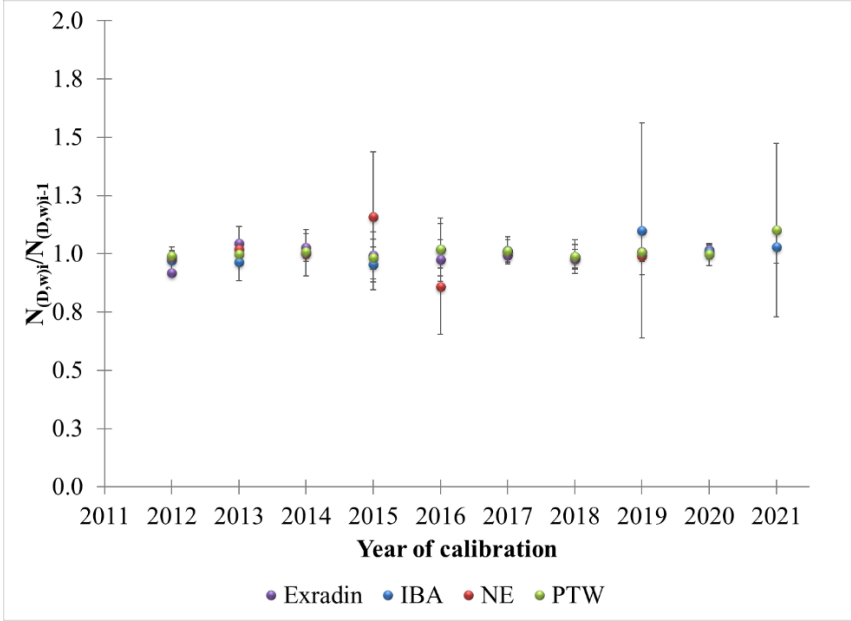


Figure 5: Variation of the ratio of the calibration coefficient from the subsequent calibration $N_{(D,w)i}$ to the calibration coefficient from the previous calibration $N_{(D,w)i-1}$ for different dosimeter manufacturers from 2012 to 2021. Error bars represent the standard deviation of the ratio

These errors most likely arise from improper handling, storage, transportation and use of the dosimeters that may result in the damage or broken of the dosimetry system. When the case was identified, additional tests were performed by the SSDL (e.g., recalibrating the dosimeter and testing the chamber with other electrometers or connecting cables). If the problem is unsolved, the abnormal behaviour was reported to the client and an investigation with the dosimeter manufacturer may need to be initiated. These findings demonstrate the importance of performing a periodic intermediate check (e.g. every month) for each calibrated dosimeter to confirm the consistency of response which could introduce confidence about the reading given in the validity calibration period [14], [18]. Moreover, these control procedures are essential either to decide whether the recalibration interval can be maintained, prolonged, or reduced or to take other

appropriate corrective actions [19].

3.4 Long-term stability of user dosimeters

In Figure 6, the frequency histogram of the long-term stabilities obtained for the dosimeters is presented. As predicted, the majority (85%) of the therapy dosimeters did not fulfil long-term stabilities within the acceptance limit of 0.5%. This discrepancy could be explained by the dosimeter response drift over time heavily used and the influence of the environment during the handling, storage, transportation, and use of the dosimeters. The mean, standard deviation, minimum, and maximum of long-term stabilities calculated for different manufacturers of dosimeters are presented in Table 3. Overall, the values ranged between 0.03% and 29.83%, with an average of 3.64%. A wide range of values between 0.84% and 17.70% were obtained for NE dosimeters indicating a significant variation in long-term stabilities.

Inspection of Shapiro-Wilk, normal Q-Q plot and box plot statistics suggested that the assumption of normality was not supported for each of the three conditions. Therefore, Spearman's rank correlation, a non-parametric test, was computed to assess the relationship between long-term stability with: (i) the year of calibration; and (ii) the manufacturer of the dosimeter. The results found that there was a negative correlation between long-term stability with the year of calibration, $r(164) = -0.081$, $p = 0.302$. The small rho coefficients, r of -0.081 , denote weak relationships, and the p -value of more than 0.05 shows evidence that there was no statistically significant correlation between these two variables. The results were supported by [10], who reported no trend of increase or decrease in the results throughout the observation. The same result was found for the relationship between long-term stability and dosimeter manufacturer, $r(164) = -1.47$, $p = 0.058$. These findings confirm the opinion that the therapy dosimeters should be calibrated every year, taking into account the unsatisfactory long-term stability of the dosimeters.

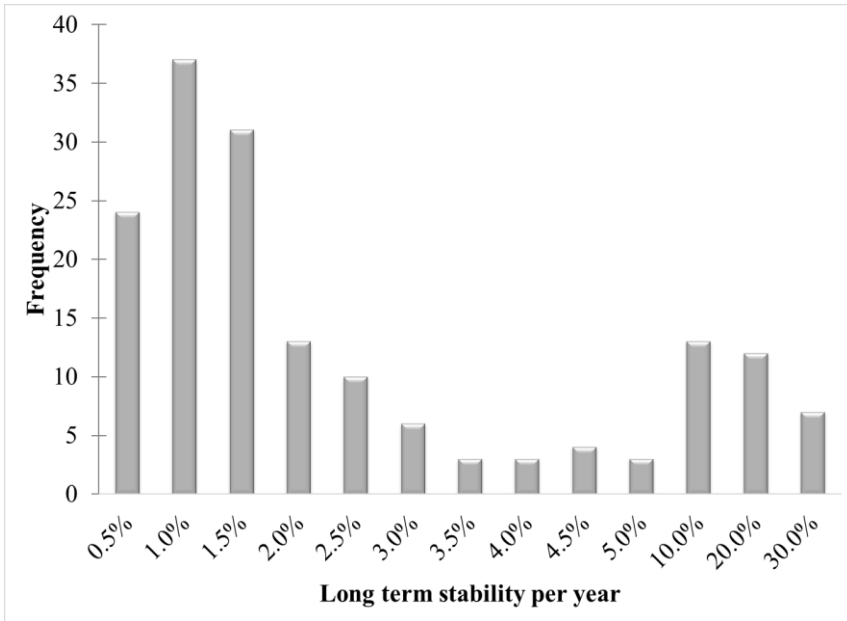


Figure 6: Distribution of the long-term stability of therapy dosimeters after calibrating several times from 2011 to 2021

Table 2: Long-term stability for different manufacturers of the therapy dosimeter

Manufacturer	Number of therapy dosimeters	Long-term stability (%)			
		Mean	Std. Dev.	Min.	Max.
Exradin	12	2.45	3.13	0.03	10.41
IBA	72	4.84	6.61	2.01	29.83
NE	4	5.55	8.18	0.84	17.79
PTW	78	2.62	4.68	0.08	26.89
Total	166	3.64	5.68	0.03	29.83

4.0 CONCLUSIONS

In conclusion, we have shown that there was a significant increment in the number of dosimeters calibrated in the SSDL from 2011 to 2021. The comparison between calibration coefficients provided by the SSDL and manufacturer demonstrates a good agreement where the majority of the user dosimeters are within the IAEA's acceptance limit of $\pm 1.5\%$. In contrast, the results of calibration coefficients and long-term stability of therapy dosimeters over these periods for different manufacturers are

not satisfied with the IAEA's acceptance limit of $\pm 0.3\%$ and 0.5% , respectively. Assessment of long-term stability yielded no statistically significant correlation between the year of calibration and the manufacturer of the dosimeter. The findings exhibit a clear preference for maintaining proper care and annual calibration of the therapy dosimeters.

5.0 ACKNOWLEDGEMENTS

This work was supported by Prototype Research Grant Scheme PRGS/1/2021/SKK07/UPM/02/1 from the Ministry of Higher Education Malaysia with the Jabatan Perkhidmatan Awam Malaysia (Hadiah Latihan Persekutuan 2021) partially funding a tuition fee.

6.0 REFERENCES

- [1] A. Azizah *et al.*, *Malaysia National Cancer Registry Report (MNCR)*. Putrajaya: Ministry of Health Malaysia, 2019. [https://www.moh.gov.my/moh/resources/Penerbitan/Laporan/Umu/2012-2016%20\(MNCRR\)/MNCR_2012-2016_FINAL_\(PUBLISHED_2019\).pdf](https://www.moh.gov.my/moh/resources/Penerbitan/Laporan/Umu/2012-2016%20(MNCRR)/MNCR_2012-2016_FINAL_(PUBLISHED_2019).pdf)
- [2] World Health Organization, "Incidence, Mortality and Prevalence by cancer site New," *Int. Agent Res. Cancer - WHO*, vol. 418, pp. 1–2, 2021. <https://gco.iarc.fr/today/data/factsheets/populations/458-malaysia-fact-sheets.pdf>
- [3] N. Yahya, N. K. Sukiman, N. A. Suhaimi, N. A. Azmi, and H. A. Manan, "How many roads must a Malaysian walk down? Mapping the accessibility of radiotherapy facilities in Malaysia," *PLoS One*, vol. 14, no. 3, pp. 1–10, 2019, doi: 10.1371/journal.pone.0213583.
- [4] Bahagian Kawalselia Radiasi Perubatan, "Senarai Radas Penyinaran Linac dan Cyberknife di Bawah Akta 304," *Portal Data Terbuka Malaysia*, 2021. <https://www.data.gov.my> (accessed Jan. 26, 2023).
- [5] Bahagian Kawalselia Radiasi Perubatan, "Statistik Bilangan Radas Penyinaran Dan Bahan Radioaktif Dalam Perkhidmatan Radioterapi," *Portal Data Terbuka Malaysia*, 2021. <https://www.data.gov.my> (accessed Jan. 26, 2023).
- [6] International Commission on Radiation Units and Measurements., "Determination of absorbed dose in a patient irradiated by beams of X or gamma rays in radiotherapy procedures," in *ICRU report 24*, 1976.
- [7] ISO/IEC, *General Requirements for The Competence of Testing and Calibration Laboratories*, 2nd Revision. Cyberjaya, Malaysia:

Department Standard of Malaysia, 2018.

- [8] Department of Standards Malaysia, "NO: SAMM 275," *The Official Website of Department of Standards Malaysia*, 2021. <https://cab.jsm.gov.my/web/guest/accredited-organisation-directories> (accessed Jan. 26, 2023).
- [9] S. B. Samat, W. Priharti, S. S. Chong, T. Kadni, and M. T. Dolah, "Stability of the absorbed dose to water calibration coefficient, ND,w for therapy level ionization chambers belonging to local radiotherapy centres: Analysis of results obtained during 2004 -2010," *Malaysian J. Anal. Sci.*, vol. 16, no. 2, pp. 142–147, 2012.
- [10] P. Ulkowski, W. Bulski, and K. Chełmiński, "Long-term stability of radiotherapy dosimeters calibrated at the Polish Secondary Standard Dosimetry Laboratory," *Appl. Radiat. Isot.*, vol. 104, pp. 181–185, Oct. 2015, doi: 10.1016/j.apradiso.2015.04.011.
- [11] A. M. Mukhtar, S. B. Samat, and M. T. Dolah, "Long Term Stability of Farmer Type Ionization Chamber Calibration Coefficient belonging to Local Radiotherapy Centres in Malaysia," *Malaysian J. Anal. Sci.*, vol. 18, no. 1, pp. 7–14, 2014.
- [12] B. R. Muir, "Ion chamber absorbed dose calibration coefficients, ND,w, measured at ADCLs: Distribution analysis and stability," *Med. Phys.*, vol. 42, no. 4, pp. 1546–1554, Mar. 2015, doi: 10.1118/1.4914381.
- [13] IAEA, *Technical Reports Series No. 398 Absorbed Dose Determination in External Beam Radiotherapy: An International Code of Practice for Dosimetry Based on Standards of Absorbed Dose to Water*. Vienna, Austria: International Atomic Energy Agency, 2000. doi: 10.1097/00004032-200111000-00017.
- [14] IAEA, *Technical Reports Series No. 469 Calibration of Reference Dosimeters for External Beam Radiotherapy*. Vienna, Austria: International Atomic Energy Agency, 2009.
- [15] NIST, "Radionuclide Half-Life Measurements," *National Institute of Standards and Technology*, 2016. <http://nist.gov/pml/data/half-life.html.cfm> (accessed Feb. 08, 2023).
- [16] Kementerian Kesihatan Malaysia, "Criteria for Applying Class H License (Certification)," *Seksyen Keselamatan Sinaran*, 2000. [http://radia.moh.gov.my/project/radiaweb/docs/criteria for applying class h license.pdf](http://radia.moh.gov.my/project/radiaweb/docs/criteria%20for%20applying%20class%20h%20license.pdf) (accessed Jan. 26, 2023).
- [17] Y. Morishita, M. Shimizu, N. Takase, W. Yamashita, and S. Sakata, "Technical note: The impact of storage humidity on the response of reference-class ionization chambers," *Med. Phys.*, vol. 49, no. 4, pp.

2725–2731, Apr. 2022, doi: 10.1002/MP.15497.

- [18] ILAC-OIML, *ILAC-G24:2022 / OIML D 10:2022 Guidelines for the Determination of Recalibration Intervals of Measuring Equipment*, E. New South Wales, Australia: International Laboratory Accreditation Cooperation and Organisation Internationale de Metrologie Legale, 2022.
- [19] A. Valcu and A. Călin, “Ensuring the validity of results by intermediate checks in the field of mass measurements,” in *J. Phys.: Conf. Ser.*, Aug. 2018, vol. 1065, no. 4, p. 042033. doi: 10.1088/1742-6596/1065/4/042033.

DEVELOPMENT OF AN IoT-BASED KNEE EXOSKELETON DEVICE FOR REHABILITATION THERAPY MONITORING

T.T.R. Thomas¹, M. R Sapiee^{2,3*}, M. H. Marhaban², A. J. Ishak²,
M. F. Miskon³

¹Quadex Automation Sdn Bhd, C-3A-03, 1, Jalan 16/11, Pusat Perdagangan
Phileo Damansara, 46350 Petaling Jaya, Selangor, Malaysia.

²Faculty of Engineering, Universiti Putra Malaysia,
43400 UPM Serdang, Selangor, Malaysia.

²Faculty of Electrical & Electronic Engineering Technology,

³Faculty of Electrical Engineering, Centre for Robotics & Industrial Automation
(CeRIA), Universiti Teknikal Malaysia Melaka, Hang Tuah Jaya, 76100 Durian Tunggal,
Melaka, Malaysia

*Corresponding Author's Email: 1mohd.razali@utem.edu.my

Article History: Received June 30, 2023; Revised July 22, 2023;
Accepted July 23, 2023

ABSTRACT: The COVID-19 pandemic has presented a multitude of challenges pertaining to medical treatments and patient care, creating a pressing need for innovative solutions. Constrained outdoor activities have hindered patients' ability to access essential healthcare, while healthcare professionals encounter difficulties in remotely monitoring and administering treatments. This study aims to address these pressing issues by proposing an Internet of Things (IoT)-based exoskeleton system designed for the monitoring of knee rehabilitation therapy. Through the utilization of the IoT platform ThingSpeak, this developed system enables patients to remotely monitor the status of their knee recovery from the comfort of their homes. The collected data is securely stored and made accessible to healthcare professionals, facilitating remote analysis and the formulation of treatment recommendations. This pioneering solution amalgamates advancements in exoskeleton technology with seamless IoT integration, establishing a dependable and easily accessible framework for the monitoring of knee rehabilitation. By empowering patients to actively participate in their own recovery process and enabling remote monitoring by healthcare providers,

this system effectively surmounts the limitations imposed by the pandemic and financial constraints. The proposed IoT-based exoskeleton system possesses the potential to revolutionize knee rehabilitation therapy, thereby enhancing patient engagement, optimizing treatment outcomes, and circumventing traditional healthcare barriers.

KEYWORDS: *Knee rehabilitation therapy; IoT-based exoskeleton; Remote monitoring*

1.0 INTRODUCTION

The knee is a highly intricate joint composed of interconnected skeletal structures, supported by ligaments and surrounded by muscles [1]. Its vital role lies in facilitating movement and providing stability to the lower extremities. Ligaments play a crucial role in stabilizing the knee, preventing excessive front-to-back movement and restricting sideways sliding [1]. Knee injuries are common, and they can cause significant impairments and pain. Knee sprains, strains, inflammation, and medical conditions like osteoarthritis are frequently observed [2]. Doctors often encounter difficulties to remotely monitor and administer treatments when patients are not present.

The integration of IoT technology in the knee rehabilitation monitoring device offers several advantages [3]. Patients can track their progress through a graphical representation, thus adjusting their rehabilitation efforts accordingly [4], [5]–[8]. This real-time monitoring empowers patients by providing immediate visual feedback on their recovery status [4]. Moreover, healthcare professionals can access patient data from other places, eliminating the need for frequent in-person visits and facilitating timely interventions and personalized care [4].

Security and privacy are important in protecting patient data and ensuring the integrity of the monitoring system [9]. Robust security measures, including encryption and authentication protocols, must be implemented to safeguard transmitted data and prevent unauthorized access [9]. These measures establish a secure and efficient platform for the IoT-based knee rehabilitation device, enabling effective monitoring and improved patient outcomes [10]–[12].

As such, the development and evaluation of an IoT-based knee rehabilitation monitoring device has been suggested. The device allows

real-time monitoring of knee recovery status, providing visual feedback to patients and enabling healthcare professionals to monitor and deliver personalized care remotely [4],[6], [13], [14].

This paper explores the development and evaluation of an IoT-based knee exoskeleton rehabilitation monitoring device [7], [8], [15]–[17]. The knee complex structure and susceptibility to injuries make it an essential focus area [1], [18]. The device provides real-time monitoring of knee recovery, empowering patients and remote personalized care [4].

2.0 METHODOLOGY

The methodology section presents the approach and procedures followed in the development and implementation of the knee rehabilitation monitoring device. This section provides an overview of the device components, operating procedures, implementation, programming, and application. The device integrates the NodeMCU microcontroller, the MPU6050 sensor, and the ThingSpeak IoT platform to enable real-time monitoring of knee movement and recovery progress [19]. The methodology outlines the steps involved in using the device, including data collection, storage, and visualization through the ThingView application. Additionally, it highlights the programming tools utilized and emphasizes the simplicity and effectiveness of the device in achieving its objectives.

2.1 Device Overview

Prior to assembling and testing the actual knee rehabilitation monitoring device, a simulation circuit as in Figure 1 is built to simulate its workability. After that, the monitoring device is developed utilizing the same components in the simulation circuit and assembled as depicted in Figure 2. The NodeMCU microcontroller is programmed to control the IoT device and transmit data to cloud storage through the ESP8266 WiFi module. The MPU6050 sensor is employed to sense knee rotational movement along the x-axis and provide its movement data. This data offers insights into the recovery progress of the knee from injuries. The data collected is stored in ThingSpeak cloud storage, allowing for future utilization. Users can access the data at any time and view it through the ThingView application on their smartphone, enabling them to monitor

movement and view graphs.

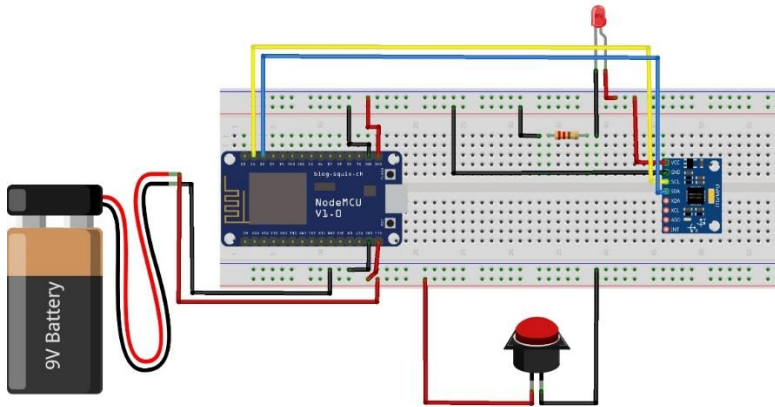


Figure 1: Simulation circuit

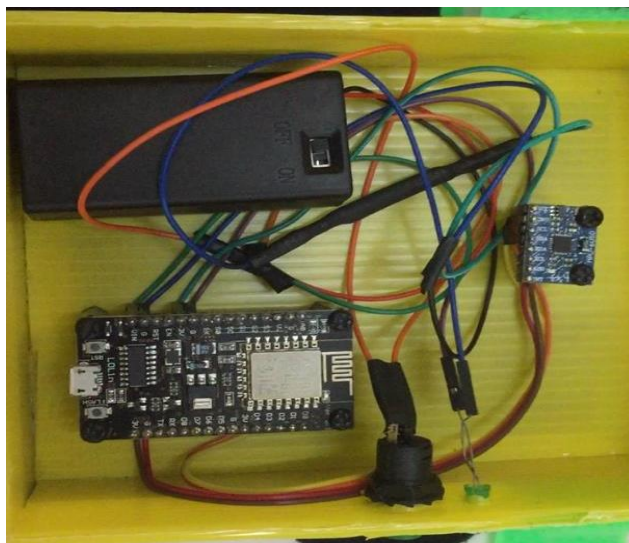


Figure 2: Assembled circuit

2.2 Operating Procedures

The following steps outline the operating procedures for the knee rehabilitation monitoring device:

- a) Activate the power supply switch to provide power to the NodeMCU.
- b) The MPU6050 sensor detects knee movement along the x-axis and converts it into a signal, which is then processed by the NodeMCU to generate meaningful data.
- c) The device transmits the data to the ThingSpeak IoT platform via a WiFi connection, where it is displayed as a continuous real-time graph.
- d) Users can access the same data through the ThingView application on their smartphones.
- e) The ThingView application presents the data in numerical form, allowing users to monitor their knee movement conveniently.
- f) Data received by the ThingSpeak platform can be downloaded in MS Excel format for further analysis or future reference.

2.3 Implementation

The knee rehabilitation monitoring device is designed to cater to IoT applications, encompassing both hardware and software components. The implementation process involves:

- a) Utilizing the Arduino IDE to update or add program codes, which can be uploaded to the NodeMCU controller via a USB cable.
- b) Connecting the NodeMCU to the ThingSpeak IoT platform, enabling the monitoring and storage of knee angle data in real-time.
- c) The ThingView application offers a real-time display of the rotational angle value obtained from ThingSpeak. It presents the instantaneous knee movement as a gauge, facilitating easy monitoring without the need for graph representation.

2.4 Programming The Device

The device programming is executed with a simple interface and essential algorithms to achieve the intended objectives and meet the its requirements. The Arduino IDE, supporting the C++ programming language, is employed to program the NodeMCU controller and establish connectivity with the ThingSpeak platform. Additionally, the NodeMCU controller can be easily integrated with other devices or

microcontrollers using a straightforward program. The value that is received from the MPU6050 is in radian. To create a graph in desired IOT platforms, the values must be converted into unit of degrees. Equation 2.1 allows the radian value to be converted into degree and incorporated in the program.

$$1 \text{ radian} = \frac{180^\circ}{\pi} \quad (2.1)$$

2.5 Applying The Device

The user needs to wear the knee support strap on the injured knee and turn on the device. Once the strap is placed, the user can start turning on the device and the WiFi to connect to the device. Once it is connected the user can start to monitor their movement by putting their knee in its initial position. Then, the user simply needs to move the knee in flexion and extension movements, shown in Figure 3.

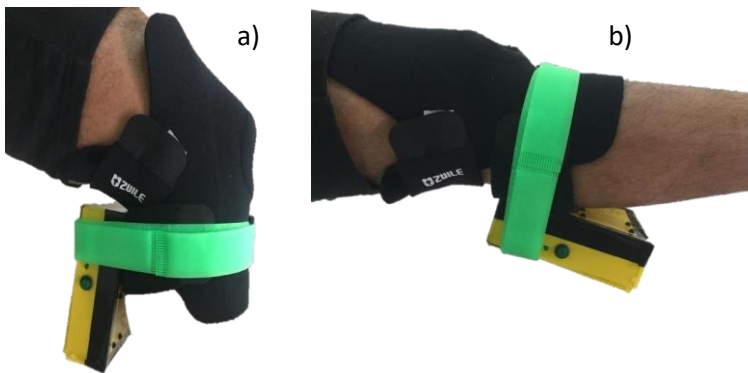


Figure 3: Knee movements with monitoring device attached a) Knee flexion
b) Knee extension

The knee movement is detected by the sensor as rotational data along the x-axis movement and directed to the device controller. The IoT platform will start to receive and collect the knee movement data from the device and start plotting a graph. Figure 4 shows the overall procedure for the device application as explained in 2.2.

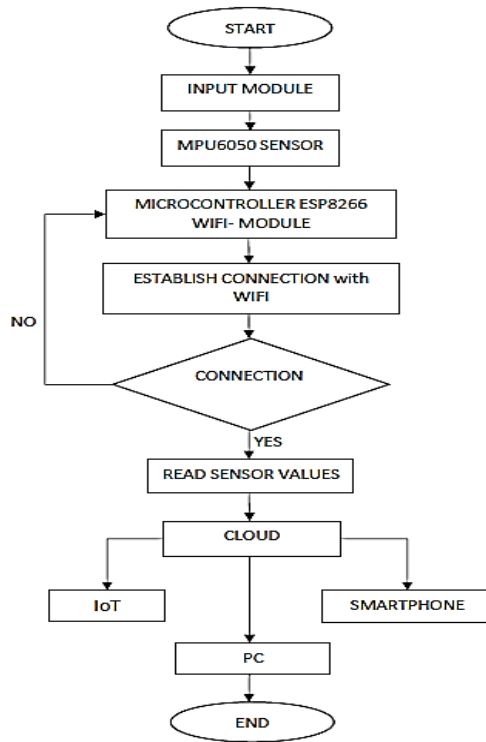


Figure 4: Device application procedure

3.0 RESULTS AND DISCUSSION

A knee rehabilitation monitoring device has been successfully developed for tracking knee recovery status. The device collected knee movement data, and displayed it on ThingSpeak's ThingView app in smartphone. The ThingSpeak smartphone app interface is as shown in Figure 5. The gauge in the application allows the user to quickly monitor the data by showing the exact current knee angle value without graph. Users could also assess the knee improvement graph through ThingSpeak web using computer as shown in Figure 6. The graph in both methods can be updated automatically or manually through web or smartphones. The collected data can then be downloaded in MS Excel format and stored for future use.

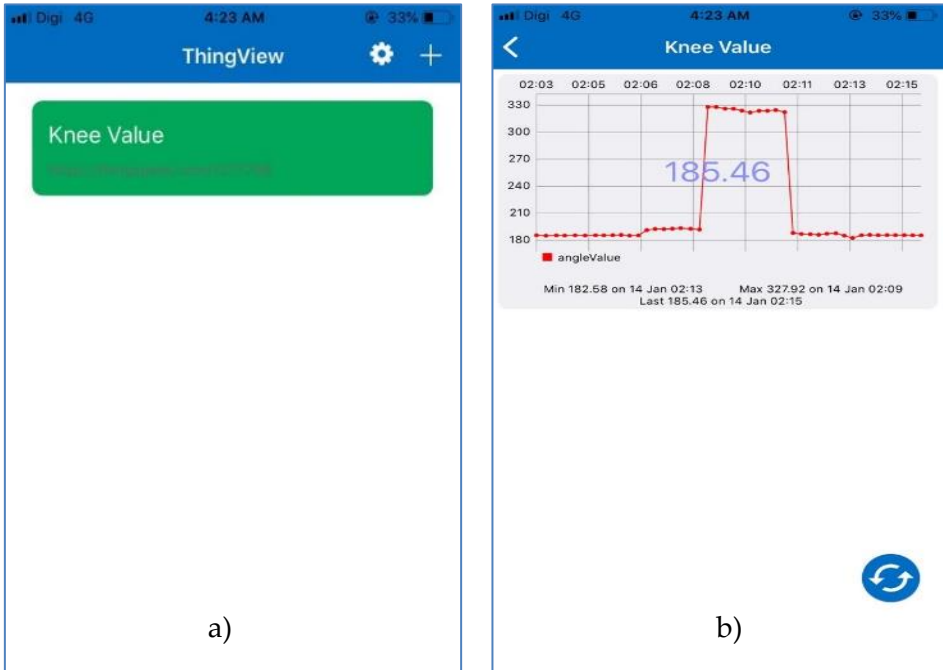


Figure 5: a) ThingView first screen b) ThingView graph display

Data collection on the knee movement angle occurred continuously, with updates at every 15 seconds. Users could monitor their knee recovery status for approximately 10 minutes in a single session. The graph on the IoT platform provided a visual representation of the knee movement data, enabling real-time assessment and comparison.



Figure 6: Knee movement graph in ThingSpeak

The device usability is enhanced by the option to download the graph as an MS Excel file for further analysis and future reference. This feature allowed users to track changes in their knee recovery over time and make informed decisions about their rehabilitation progress.

4.0 CONCLUSION

A knee rehabilitation monitoring device that allows the patient to view knee recovery status and the doctor to track the data remotely has been developed. Moreover, it has been developed by combining the features of the components with IoT. The device has been successfully tested for various angles in many situations and its data visualized as graph on the ThingSpeak IoT platform, provided a clear and measurable representation of the knee's improvement over time. The real-time monitoring of the knee angle and its progression enables personalized care and tailored rehabilitation efforts, allowing patients to adjust their exercises based on the immediate feedback provided by the graph.

In conclusion, the developed device tracks the knee's movement angle and recovery progress over time. By attaching the device to their knee, patients can undergo real-time monitoring of knee flexion and extension movements. The real-time graph visualization and data storage capabilities provided valuable insights for users to track and evaluate their knee rehabilitation progress. The knee rehabilitation monitoring device, utilizing the NodeMCU microcontroller, MPU6050 sensor, and ThingSpeak IoT platform, offered an effective solution for monitoring knee recovery. In the future, the device can be integrated into a modular knee exoskeleton, thus contributing to effective self-monitoring for knee rehabilitation therapy.

5.0 ACKNOWLEDGMENTS

The authors would like to express appreciation to Universiti Teknikal Malaysia Melaka (UTeM) and Universiti Putra Malaysia (UPM) for their full support.

6.0 REFERENCES

- [1] J. Jensen, L. Lundin-Olsson, L. Nyberg, and Y. Gustafson, "Falls among frail

- older people in residential care," *Scandinavian Journal of Public Health*, vol. 30, no. 1, 2002.
- [2] D. Rabago *et al.*, "Hypertonic dextrose injections (prolotherapy) for knee osteoarthritis: Results of a single-arm uncontrolled study with 1-year follow-up," *Journal of Alternative and Complementary Medicine*, vol. 18, no. 4, 2012.
- [3] M. M. M. Al-Omri, N. A. M. Alduais, M. N. Adon, A.-M. H. Y. Saad, A. S. H. Abdul-Qawy, and T. Sutikno, "Internet of things-based telemonitoring rehabilitation system for knee injuries," *Bulletin of Electrical Engineering and Informatics*, vol. 9, no. 6, pp. 2658–2666, 2020.
- [4] C. Freeman, D. Tong, K. Meadmore, A. M. Hughes, E. Rogers, and J. Burridge, "FES based rehabilitation of the upper limb using input/output linearization and ILC," in *Proceedings of the American Control Conference*, 2012.
- [5] K. Sengchuai *et al.*, "Development of a Real-Time Knee Extension Monitoring and Rehabilitation System: Range of Motion and Surface EMG Measurement and Evaluation," in *Healthcare*, 2022, vol. 10, no. 12, p. 2544.
- [6] A. Akbari, F. Haghverd, and S. Behbahani, "Robotic home-based rehabilitation systems design: from a literature review to a conceptual framework for community-based remote therapy during COVID-19 pandemic," *Frontiers in Robotics and AI*, vol. 8, p. 612331, 2021.
- [7] E. Mora-Tola, J. Loja-Duchi, A. Ordonez-Torres, A. Vazquez-Rodas, F. Astudillo-Salinas, and L. I. Minchala, "Robotic knee exoskeleton prototype to assist patients in gait rehabilitation," *IEEE Latin America Transactions*, vol. 18, no. 9, 2020.
- [8] S. F. Ahmed *et al.*, "Robotic exoskeleton control for lower limb rehabilitation of knee joint," *International Journal of Engineering and Technology (UAE)*, vol. 7, no. 2.34, 2018.
- [9] K. Gatsis and G. J. Pappas, "Poster abstract: Wireless control for the IoT: Power, spectrum, and security challenges," in *Proceedings - 2017 IEEE/ACM 2nd International Conference on Internet-of-Things Design and Implementation, IoTDI 2017 (part of CPS Week)*, 2017.
- [10] S. Y. Y. Tun, S. Madanian, and F. Mirza, "Internet of things (IoT) applications for elderly care: a reflective review," *Aging clinical and experimental research*, vol. 33, pp. 855–867, 2021.
- [11] A. J. Perez, F. Siddiqui, S. Zeadally, and D. Lane, "A review of IoT systems to enable independence for the elderly and disabled individuals," *Internet of Things (Netherlands)*, vol. 21, 2023.
- [12] A. Anand, S. P. Mishra, and S. Sahana, "Assistive devices and IoT in healthcare functions," *Deep Learning and IoT in Healthcare Systems: Paradigms and Applications*, vol. 103, 2021.

- [13] S. F. Atashzar, J. Carriere, and M. Tavakoli, "Review: How Can Intelligent Robots and Smart Mechatronic Modules Facilitate Remote Assessment, Assistance, and Rehabilitation for Isolated Adults With Neuro-Musculoskeletal Conditions?," *Frontiers in Robotics and AI*, vol. 8, 2021.
- [14] I. Ahmad *et al.*, "Emerging Technologies for Next Generation Remote Health Care and Assisted Living," *IEEE Access*, vol. 10, pp. 56094–56132, 2022.
- [15] G. M. Bryan, P. W. Franks, S. C. Klein, R. J. Peuchen, and S. H. Collins, "A hip–knee–ankle exoskeleton emulator for studying gait assistance," *International Journal of Robotics Research*, 2020.
- [16] M. Kumar and K. Bowal, "Exoskeleton for Knee Arthritis Patients," *Journal of Student Research*, vol. 10, no. 4, 2021.
- [17] Y. Wang, Z. Liu, and L. Shi, "Development of an Exoskeleton Rehabilitation Robot Framework for the Knee Joint Based on Predictive Assessment," *IEEE Access*, vol. 9, pp. 168794–168805, 2021.
- [18] E. Sejdíć, A. Godfrey, W. McIlroy, and M. Montero-Odasso, "Engineering human gait and the potential role of wearable sensors to monitor falls," *Falls and Cognition in Older Persons: Fundamentals, Assessment and Therapeutic Options*, pp. 401–426, 2020.
- [19] A. Moore, M. Mehrubeoglu, A. Mooney, and L. McLaughlan, "Application of IoT-based sensing and signal processing for rehabilitation," in *Signal Processing, Sensor/Information Fusion, and Target Recognition XXXI*, 2022, vol. 12122, pp. 287–297.

DOSE MAP BLOOD IRRADIATOR DOSIMETRY SYSTEM: CUSTOMIZED BLOOD EQUIVALENT PHANTOM AND GAFCHROMIC EBT-XD FILM

A.S.Fazad^{1,2}, N.M.Noor^{1,2}, M.A.Nasir³

¹Medical Physics Laboratory, Department of Radiology, Faculty of Medicine and Health Sciences, Universiti Putra Malaysia, 43400, Serdang, Selangor, Malaysia.

²Medical Physics Unit, Hospital Sultan Abdul Aziz Shah, 43400, Serdang, Selangor, Malaysia

³Faculty of Science and Technology, Universiti Kebangsaan Malaysia, 43600 Bangi, Selangor, Malaysia.

*Corresponding Author's Email: ^{1,2}noramaliza@upm.edu.my

Article History: Received July 13, 2023; Revised July 30, 2023;
Accepted July 30, 2023

ABSTRACT: Blood irradiation is done to sterilize and cease donor T-lymphocytes functionality to avoid Transfusion Associated-Graft Versus Host Disease (TA-GVHD). Dose mapping is the primary means of ensuring that the irradiation process is being conducted correctly. The aim of this study is to measure the minimum, maximum and central absorbed gamma radiation dose delivered at the newly customized blood equivalent phantom using a Gafchromic EBT-XD film. A Gammacell 3000 Elan Blood Irradiator with Cesium-137 source was used. To obtain the dose calibration curves, the films were placed at the center of a phantom and irradiated with the dose range from 5 Gy to 35 Gy with one unirradiated film as a control. The dose calibration curve was plotted using red, green and blue channels. For the dose mapping measurement, the irradiation exposure of 9.03 minutes was used to deliver a central dose of 25 Gy to the film. The response of the film will be compared with the GC Dose Mapping Report 2022 which used a water equivalent medium as a phantom. For the calibration curve, the red channel of the film was utilized in this study as it had a higher signal than the other channel. The doses obtained at central, minimum and maximum using EBT-XD film with customized blood equivalent phantom were in agreement with that obtained from GC Dose Mapping Report 2022 to be within $\pm 7.6\%$, $\pm 8.51\%$ and $\pm 9.95\%$ respectively. We concluded that the customized blood equivalent phantom together with EBT-XD film has a potential to map the dose in blood irradiator accurately. The doses obtained from EBT-XD film were in the range of doses needed to inhibit the proliferation of the T-lymphocytes with central, minimum and maximum doses (26.9 Gy, 17.2 Gy, 35.7 Gy).

KEYWORDS: *Blood Irradiator, Cesium-137, Gafchromic EBT-XD Film, Dose Map, Blood Equivalent Phantom*

1.0 INTRODUCTION

Blood transfusion is a vital component of every country's health service. It can be a life-saving intervention for severe, acute anemia, but mistakes in the transfusion process can be life-threatening, either immediately or years later through transmission of infectious agents [1]. For example, transfusion associated-graft versus host disease (TA-GVHD) which is identifies as an uncommon disease that could occur after an unirradiated blood transfusion to immunocompromised recipient such as bone marrow transplant patients, patients with malignancies receiving aggressive chemotherapy and persons with congenital immune deficiency syndromes, where the recipient's immune responses are incapable of effectively eliminating donor leukocytes, permitting unabated responses of the donor T-lymphocytes [2].

Blood irradiation is done to sterilize and cease donor T-lymphocytes functionality to avoid immunological reaction where it triggers hostile reaction due to presence of foreign cells from the recipient's body. This disease is known as TA-GVHD) and is treated by utilizing of at least 25 Gy to 50 Gy gamma irradiation from either Cs-137 or Co-60 using a specialized irradiation machine called blood irradiator, enough even for use towards pediatrics and transplant patients [3]. Sterilization of T-lymphocytes is done by damaging its Deoxyribonucleic Acid (DNA) and arrest responses to allogeneic cells [4]. Utilization other than gamma sources for T-cells sterilization are also viable for X-rays that includes self-constrained X-ray (bremsstrahlung), medical linear X-ray (bremsstrahlung), and electron accelerators used primarily for radiotherapy [4,5].

Dose mapping is the primary means to ensure that the irradiation process is being conducted correctly by measuring the maximum and minimum delivery of radiation within a simulated blood component over an area in which a blood component is placed. To achieve this, dose mapping should be performed with sensitive dosimetry techniques [6].

Film dosimeters are often used to map dose in blood irradiators and EBT-XD film is the most appropriate dosimeter for dose verification [3]. Radiochromic film approach, radiation sensitive film is embedded

between two halves of a circular-fitting polystyrene plastic phantom [5].

Moroff et al 1997 [6] reported that in practical terms, attenuation is caused when the irradiation enters a liquid, such as water or blood, and will increase as the irradiation transverses to the center point. The edges of the canister are exposed to a greater dose of irradiation compared with the center line because the attenuation is less in the periphery. The generated dose map describes the distribution of the dose, and it is commonly observed in actual practice that the minimum dose is located at the central bottom of the canister.

The dose delivery in irradiation processes is influenced by various physical factors, such as the geometry of the source and sample, the uniformity of the dose distribution within the irradiation volume, and the dose absorption in the sample. Fearon et al 2005 [7] reported that the greatest influence on the dose delivered to the blood product is the source and sample geometry. Therefore, it is importance to perform routine dose validation as recommended by Department of Health and Human Services (1993).

In this study the main objective is to investigate the uniformity of the dosage of radiation delivered to the blood using Caesium-137 (Cs-137) gamma source blood irradiator with newly customized blood equivalent phantom using Gafchromic EBT-XD by examining the integrity of central, minimum, and maximum doses. It is important to ensure that the given doses are sufficient to prevent graft-versus-host disease in both pediatric and transplant patients. The dose differences is compared to the irradiation results from the previous GC Dose Mapping Report 2022 by using water equivalent phantom [8]. The final results shall conclude the suitable phantom to be utilized when undergoing a clinical experiment or routine dose validation of blood irradiator quality control activities.

2.0 METHODOLOGY

2.1 SAMPLE PREPARATION AND IRRADIATION

For this study the Gammacell 3000 Elan Blood Irradiator located at the Department of Pathology, Hospital Sultan Abdul Aziz Shah (HSAAS) was used. The Gamma irradiation chamber (GIC) components included are a metal canister that is positioned on a rotating turntable with pre-fixed rotational speed, and a free standing pencil-shaped Cs-137 irradiator as gamma source positioned vertically and is operating at 30.9 Terabecquerel (TBq) equivalent to 8.35 Curie (Ci).

The customized blood-equivalent phantom (CIRS Inc, USA) shown in Figure 1, with a density of 1.06 g/cm^3 , was used to closely mimic real-life clinical irradiation conditions and act as a substitute for blood. This phantom allows for the calibration of photon and electron beams within 0.5% of true water dose, making it ideal for routine beam constancy inspection.

To create two hemispheric-shaped phantoms of identical size and dimensions, a cylindrical phantom with a diameter of 12 cm and a height of 18 cm was vertically cut from top to bottom. This cutting process allowed for the insertion of Gafchromic EBT-XD films for further evaluation.



Figure 1: Customized blood equivalent phantom

2.2 FILM DOSE CALIBRATION

The EBT-XD Gafchromic films were cut into eight small cuts of $2 \text{ cm} \times 2 \text{ cm}$ square and three large cuts of $8 \text{ cm} \times 18 \text{ cm}$ rectangle. The films are prepared for calibration curve and dose mapping purposes respectively, where each part has one unirradiated film to act as a control. The films are suitable for absorbed dose measurement of high energy photons. The films are composed of a nominally $25 \mu\text{m}$ thick active layer sandwiched in between two $125 \mu\text{m}$ matte-polyester substrates which are unneeded for post-exposure treatment. The active layer contains the active component, a marker dye, stabilizers, and other components giving the film its near energy-independent response [9]. The thickness of the active layer will vary slightly between different production lots. The EBT-XD film has a functional dynamic

dose range of 0.1 Gy to 60 Gy, and an efficient optimum dose range of 0.4 Gy to 40 Gy. A highly efficient and effective radiochromic dosimetry system as it has more decreased UV/light sensitivity than its predecessors and unnecessary for non-uniformity correction due to addition of marker dye in the film active layer.

The EBT-XD film dose calibration curve technique implemented was, by irradiating seven out of eight small 2 cm × 2 cm Gafchromic EBT-XD films inside the free-standing Cs-137 sourced blood irradiator. The films were sandwiched in between the hemispheric blood equivalent phantom and positioned at the center of the phantom. Each film was irradiated once at doses of 5 Gy, 10 Gy, 15 Gy, 20 Gy, 25 Gy, 30 Gy, and, 35 Gy. One film is left unirradiated to provide comparison as a control sample during measurement.

The films were placed at the centre inside the blood equivalent phantom then they were sealed from the outside using thin micropore tape to avoid being dislodged during irradiation. After irradiation, the topside of the films is labeled for reference and left for cooling.

The small films are scanned in transmission mode, with no color or sharpness corrections and consistent orientation using a light emitting diode (LED) based flatbed with 48-bit (16-bit per channel) color Microtek ScanMaker 1000 XL (Taiwan) scanner that have three color modes consisting of red, green, and blue color with a resolution of 75 dots per inch (dpi). Scanning was done on the small films with fixed position and saved as tiff. image. The pixel values of the images were then analyzed using ImageJ by draw the ROI with five 0.52 cm × 0.52 cm squares.

The pixel values are translated into net optical density (OD) using Equation 1 and are used to plot the dose calibration graph.

$$\text{Net OD} = \text{OD}_{\text{exposed}} - \text{OD}_{\text{unexposed}} = \log_{10} \left(\frac{I_{\text{unexposed}}}{I_{\text{exposed}}} \right) \dots (1)$$

where $I_{\text{unexposed}}$ and I_{exposed} are the readings for unexposed and exposed film pieces, respectively [10].

The dose calibration curves of the films (net OD versus absorbed dose) were plotted individually according to their respective color channels using the RGB channels scan modes to present and choose the best channel to obtain the optimum curves for the films.

2.3 FILM DOSE MAPPING

Absorbed dose mapping was conducted based on the net OD average from two 8 cm × 18 cm sized EBT-XD films. Extrapolation of net OD versus absorbed dose calibration graph is utilized to obtain the absorbed dose of each 1 cm × 1 cm region of the EBT-XD film. This method is done accurately by using the quadratic equation of the best polynomial curve that is close to unity.

3.0 RESULTS AND DISCUSSION

3.1 FILM DOSE CALIBRATION

"The calibration curves obtained for the red, green, and blue channels against an absorbed dose range from 0 to 35 Gy are shown in Figures 2. Based on Figure 2, at doses of 20 Gy and above, the green and yellow channels displayed decreasing OD values as the dose increased. This result contradicts the report written by Palmer et al. in 2015 [11], where the optical density increased with an increasing dose. Higher doses of optical density were applied gradually until saturation was reached. For the red channel, it showed sensitivity at higher dose levels compared to the green and yellow channels, with a net OD value higher than the other channels."

The red channel polynomial curve was found to be the most relevant to be used as net OD versus absorbed dose calibration curve as its goodness-of-fit measure of R^2 is 0.9971, the closest to unity, which is 1. This is followed by the green channel with an R^2 value of 0.9777, and finally the blue channel with an R^2 of 0.8150. The slopes of the response function for the EBT-XD film have shown that the red channel has a broader dynamic range than the other channels. This means that the red channel is significantly more sensitive than the others. Therefore, this study used the red channel of the EBT-XD film since it had a greater dynamic range.

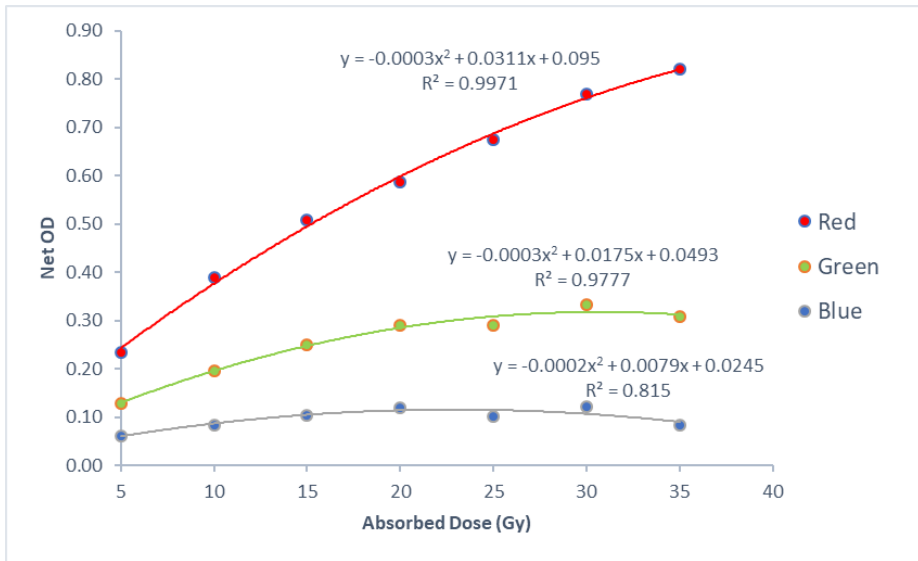


Figure 2: Calibration curve of red, green, and blue channels on Gafchromic EBT-XD films.

3.2 FILM DOSE MAPPING

Extrapolation of films absorbed dose through net OD relationship using red color channel polynomial curved calibration graph made the absorbed dose mapping of large films possible.

By utilizing the OriginPro 2022 software, both Figures 3 and 4 depict color and black-and-white contours. Figure 3 presents the outcomes of the Experimental: Dose mapping of Gafchromic EBT-XD film using the customized blood-equivalent phantom, while Figure 4 shows the results of the GC dose report 2022: Dose Mapping Gafchromic EBT-XD film using the water-equivalent phantom. The colored contour graph on the film is created using red, green, and blue color spectra, representing the absorbed dose of both films. This facilitates dose distribution analysis

From Figure 3, 25 Gy irradiation dose distribution on films were shown to be approximately 25 Gy or larger. In this experiment the absorbed dose at the center of the film is found to be 26.9 Gy, with a central absorbed dose rate of 2.99 Gy/min. The minimum and maximum doses for current study of Gafchromic EBT-XD film irradiation using customized blood equivalent phantom are found to be 17.2 Gy and 35.7 Gy respectively. On the other hand, the results using water equivalent phantom shows that the absorbed dose at the center of the film is 25 Gy with a central absorbed dose rate of 2.78

Gy/min. The minimum and maximum doses are found to be 19.1 Gy and 32.9 Gy respectively.

The maximum dose is located on the most left bottom side of the film since the most affected areas should be on the periphery horizontal sides, while the minimum dose is located on the top side of the film as should on the vertical sides. This is due to the sided irradiation condition by the singular pencil vertically configured Cs-137 source in the blood irradiator [6]. As we can observe from Figure 3 and 4, it is in agreement with Moroff et al 1997 [6] that where areas affected more are at the periphery of the film compared to the center as it is less attenuated by the blood equivalent phantom.

The minimum and maximum absorbed dose range for both figures are different due to the slightly extended period of irradiation for the current study and difference in phantom handling. Overall, from both results, there is a susceptible amount of absorbed dose present at the center of the film to sterilize and halt t-lymphocytes functionality which is 25 Gy [12].

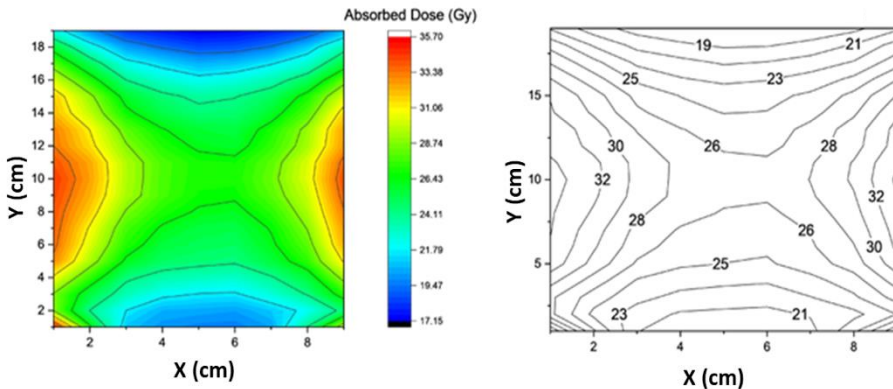


Figure 3: Experimental: Dose mapping of Gafchromic EBT-XD film using customized blood-equivalent phantom; (a) color contour and (b) black and white contour.

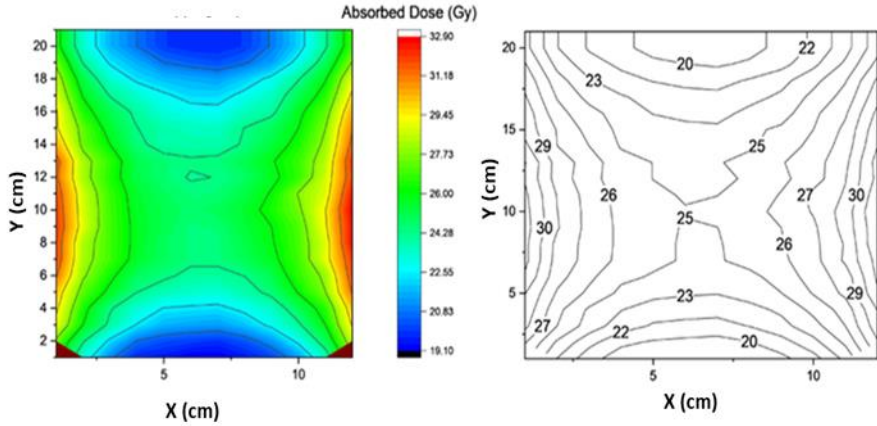


Figure 4: GC dose report 2022: Dose mapping of Gafchromic EBT-XD film using water-equivalent phantom; (a) color contour and (b) black and white contour.

Table 1 summarizes the central, minimum and maximum dose according to experimental using blood equivalent phantom and GC dose mapping report 2022 using water equivalent phantom. The doses obtained at central, minimum and maximum using EBT-XD film with customized blood equivalent phantom were in agreement with that obtained from GC Dose Mapping Report 2022 with water equivalent phantom [8, 13] where the deviations are $\pm 7.6\%$, $\pm 8.51\%$ and $\pm 9.95\%$ respectively.

Type	Central Dose (Gy)	Central Dose Rate (Gy/ minute)	Maximum Dose (Gy)	Minimum Dose (Gy)
Gafchromic EBT-XD Films (Blood Equivalent Phantom)	26.9	2.99	35.7	17.2
GC Dose Mapping Report, 2022 Gafchromic EBT-XD Films	25.0	2.78	32.9	19.1

(Water Equivalent Phantom)				
Deviation (%)	±7.6	±7.55	±8.51	±9.95

Table 1: Dose for central and dose rate, maximum and minimum dose

4.0 CONCLUSION

The experimental Gafchromic EBT-XD film showed central, minimum, and maximum doses of 26.9 Gy, 17.2 Gy, and 35.7 Gy, respectively. These doses fall within the acceptable range for blood irradiation, which is typically 15 Gy to 50 Gy. The doses obtained at the central, minimum, and maximum positions using the EBT-XD film with the customized blood-equivalent phantom were in agreement with those obtained from the GC Dose Mapping Report 2022, with deviations of ±7.6%, ±8.51%, and ±9.95%, respectively.

Based on the current findings, the customized blood-equivalent phantom offers a highly accurate method for mapping the absorbed dose in a blood irradiator. The use of EBT-XD film for dose mapping with the blood-equivalent phantom is justified by the fact that the measured doses on the film fall within the range necessary to inhibit T-lymphocyte proliferation.

5.0 REFERENCES

- [1] Bates, I., & Owusu-ofori, S. (2020). Blood Transfusion. In System-oriented Disease, 229–234.
- [2] Fast, L. D. (2015). Preventing transfusion-Associated graft-versus-host disease: state of the art. International Journal of Clinical Transfusion Medicine, (2), 1–6.

- [3] Syafinaz, N, Mohd Roslee, A. Nur Amalina, & M. N. Noramaliza. (2020.) Dose Mapping of Gamma Irradiation Chamber (GIC). *Asian Journal of Medical Technology (AJMedTech)* 2(1): 49-57.
- [4] Gões, E. G., Borges, J. C., Covas, D. T., Orellana, M. D., Palma, P. V. B., Morais, F. R., & Pelá, C. A. (2006). Quality Control of Blood Irradiation: Determination T Cells Radiosensitivity To Cobalt-60 Gamma Rays.
- [5] Saglam, S., Cakir, A., & Seyfettin, K. (2011). Blood Irradiation. In *Modern Approaches To Quality Control* (pp. 335–347). Retrieved from <http://www.intechopen.com/books/modern-approaches-to-quality-control/blood-irradiation>
- [6] Moroff, G., & Luban, N. L. . (1997). The Irradiation of Blood and Blood Components to Prevent Graft-Versus-Host Disease: Technical Issues and Guidelines. *Transfusion Medicine Reviews*, 11(1), 15–26
- [7] T. Fearon, V. R. Criss, and N. L. C. Luban, “Blood irradiator dosimetry with BANG polymer gels,” vol. 45, pp. 1658–1662, 2005.
- [8] Best Theratronics Dosimetry Laboratory. (2022). GC 3000 Dose Mapping Report, Best Theratronics Ltd., Canada, 1-3.
- [9] Ashland. Gafchromic™ EBT-XD films. <https://www.ashland.com/industries/medical/radiotherapy-films/ebtxd>
- [10] Dreindl, R., Georg, D., & Stock, M. (2014). Radiochromic film dosimetry: considerations on precision and accuracy for EBT2 and EBT3 type films. *Zeitschrift für Medizinische Physik*, 24(2), 153-163.
- [11] Palmer, A. L., Dimitriadis, A., Nisbet, A., & Clark, C. H. (2015). Evaluation of Gafchromic EBT-XD film, with comparison to EBT3 film, and application in high dose radiotherapy verification. *Physics in Medicine & Biology*, 60(22), 8741.
- [12] Olivo, R. A., Silva, M. V. D., Garcia, F. B., Soares, S., Rodrigues, V., & Moraes-Souza, H. (2015). Evaluation of the effectiveness of packed red blood cell irradiation by a linear accelerator. *Revista brasileira de hematologia e hemoterapia*, 37, 153-159.
- [13] K.S.A.K. Bakar, N.M. Noor, M.F. Hassan, F. Idris, D.A. Bradley. (2023). Dose mapping in Cesium-137 blood irradiator using novel Ge-doped silica optical fibres in comparison with gafchromic EBT-XD film: A preliminary study, *Radiation Physics and Chemistry*, 209, 111010